University of Tartu
Institute of Technology
Intelligent Materials and Systems Laboratory

Materials Science and Technology

Master's Thesis (30 ECTS)

A mm-scale liquid-enabled robotic exoskeleton

Author:
Kadri-Ann Valdur

Supervisors:
Indrek Must
Tarmo Tamm

June 4, 2021

Fact sheet

A mm-scale liquid-enabled robotic exoskeleton

Liquid has paramount importance in every living organism, sometimes with interesting multi-functionality, e.g. in spiders. This work aims to understand the benefits and critical factors of liquid enabled exoskeletons with internal muscles in mm-scale for possible robotics implementation. For this, electrochemically active tube-shaped linear polypyrrole (PPy) actuator was combined with an inactive variable stiffness two photon polymerised (2PP) IP-Q photoresist exoskeleton immersed in propylene carbonate (PC). Model-based design of continuous exoskeletons with the characterised parameters resulted in two configurations based on the movement direction of the pulling force of the PPy artificial muscle - to-bend and to-straighten. The passive exoskeleton and active muscle configuration in the to-bend version resulted in a maximum of 15° and 5° angle. Future perspective of vascular soft robotics with robotic blood can be foreseen.

Keywords: soft robotics, bioinpired, exoskeleton, actuator, polypyrrole, conductive polymer actuator, movement analysis

CERCS code: T150 - material technology; T390 - polymer technology, biopolymers

Millimeetriskaalas vedelikvõimaldatud robootiline eksoskelett

Igas elusorganismis on tähtis roll vedelikul ning see võib olla multifunktsionaalne nagu nt ämblikes. Töös iseloomustati ämblikutest inspireeritud pidevat eksoskeletti, mille tööd võimaldab multifunktsionaalne vedelik. Selleks iseloomustati esiteks elektrokeemiliselt sünteesitud torukujulise polüpürrooli (PPy) täiturmehhanismi ja propüleenkarbonaadiga (PC) immutatud kahe footon polümerisatsiooniga (2PP) polümeriseeritud fotoresisti IP-Q elastsusomadusi. Iseloomustatud parameetritega pidevate eksoskelettide simuleerimise

abil saadi PPy kunstlihase tõmbejõu liikumissuunal põhinevad konfiguratsioonid - painutus ning sirutus. Mitteaktiivse eksoskeleti ja aktiivse lihase konfiguratsiooni korral painutusega versioonis saavutati maksimaalne ja tüüpiline paindenurk vastavalt 15 ja 5 kraadi. Tulevikuperspektiiviks on võimalik ette näha rakendusi näiteks robotverega vaskulaarses pehmerobootikas.

Märksõnad: pehmerobootika, bioinspiratsioon, eksoskelett, täitur, polüpürrool, juhtivpolümeertäitur, liikumisanalüüs

CERCS kood: T150 - materjalitehnoloogia; T390 - polümeeride tehnoloogia, biopolümeerid

Contents

Introduction

After several billions of years, Nature has experience developing organisms, materials and mechanisms with impressive efficiency. Making use of this, bioinspiration is an approach where biological systems are used as a source of inspiration for various technical solutions. For example, bullet trains inspired by kingfishers, hydrophobic surfaces inspired by the lotus leaf or Velcro inspired by burdock burrs are just some examples of Nature's design put into technical use.

When finding a suitable biological model, the high functionality in the researched application is paramount. In a broader view, there would not be life without water. More specifically, liquid enables life as often water is the primary solvent in a solution with inorganic (salts, minerals etc.) and organic (proteins, enzymes, etc.) parts. Liquid can be used as a living habitat (oceans, lakes), nutrient transportation medium (blood) or even as a tool (hunting archerfish). To be inspired by the (multi)functionality of liquid in life can be a winning method.

One of the many multi-functional uses of liquid can be found in small organisms with continuous exoskeletons, such as spiders. The delicate limbs are enabled by liquid with hydration dependent stiffness of the exoskeleton and haemolymph (the spider equivalent of blood) used for nutrient transportation and critical joint extension.

This work aims to understand the benefits and critical factors of mm-scale functional liquid enabled actuation of compliant continuous exoskeletons with internal artificial muscles. For this, based on the spider as a model organism, two photon polymerised (2PP) continuous structures are immersed in a functional electrolyte to increase compliance and actuated with ionic electroactive polymer polypyrrole. Simulations are used to determine the effective elastic modulus of the immersed structures and aid the joint's design. The performance of the joint is analysed.

The reader can find the literature review about bioinspiration, exoskeletons and technologies for milli-scale robotics in the first chapter. Next is the aim and approach of this work with the concept. In the third chapter, the workflow, fabrication and characterisation

methods for electrochemical synthesis, 2PP and simulations are described. The fourth and final chapter is devoted to the results and discussion of this work.

This thesis is a part of an international collaboration with the Italian Institute of Technology (IIT) Bioinspired Soft Robotics Center led by Barbara Mazzolai, PhD and Intelligent Materials and Systems (IMS) laboratory in the University of Tartu. The author worked closely with Edoardo Sinibaldi, PhD and Isabella Fiorello.

1 Literature overview

1.1 Inspiration

1.1.1 Bioinspiration from Liquid Enabled Life

Life has evolved on Earth for billions of years, and that process has optimised the functionality of all living beings. Thus, it is an excellent source of inspiration for scientists and artists for practical application. By studying biological models, it is possible to gain insight into more effective designs and functions. One success story is the invention of a common mechanical attachment strip, Velcro, by a Swiss engineer George de Mestral [1, 2] who found the inspiration from burdock burrs on a regular walk with his dog. He not only found and studied the biological mechanism but adapted it to perform superbly with known and yet unknown technological methods. This allowed the invention to be produced *en masse* and in a cost-effective manner with widespread applications to follow.

The key part in bioinspiration is defining and abstracting the solutions in contrast to biomimicry which is the copying of the exact materials and morphologies in Nature [1]. It is not always necessary, reasonable or possible to copy naturally occurring materials or structures. As with the Velcro example - the exact materials were not copied, and by implementing state-of-the-art technologies, a solution with high functionality was born. The general process of bioinspired design with the example of robotics is described in figure 1.1. What is important to notice is the circular workflow of the process - inspiration to abstraction to implementation and back again to inspiration.

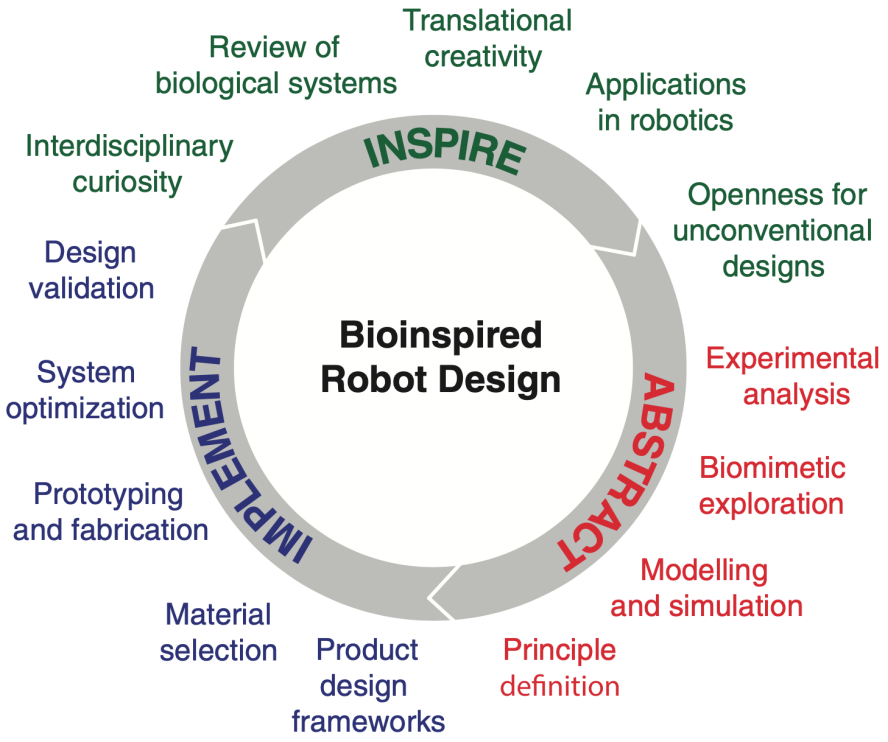

FIGURE 1.1: The bioinspired robot design process that could be applied to other applications as well [1]

Most living organisms are enabled by liquid - may it be the ocean as a living habitat, blood as oxygen, carbon dioxide and nutrient transportation medium, or water as a means to hunt prey by archerfish [3]. Such ample use of liquid in life gives plenty of reason to be inspired by its multi-functionality. Liquid can enable actuation in many ways - one interesting being the spiders' dual-actuated joints with hydraulic pressure used for extension [4] as well as for the hydration of the exoskeleton [5] and nutrient transportation.

1.1.2 Case Study - Spiders

Spiders are versatile arthropods with interesting abilities. In addition to their unique capability of weaving complex webs with various shapes, sizes and functions, their locomotion and movement mechanism has been an inspiration for various technical appliances for close to 50 years [6]. This interest has resulted in plenty of information sources like

books and articles ([4, 6–9] to name a few), making the spider a relatively easy subject to study as a biological model for robotic application.

The spider leg has seven leg joints [4] which control the positioning of the leg (see fig 1.2). Mobility is determined by the musculature as well as the type of joint. Ball joints with multiple degrees of freedom are found near the trunk, with most of the many muscles required to operate the joints located in the body instead of the limbs themselves. Hinge joints are found in the middle portion of the leg as they do not need muscles for stabilisation perpendicular to the main movement plane. Most distal joints are often actuated with long tendons. [10] The musculature does not vary greatly between different species of spiders - there tends to be around 30 different leg muscles in a single spider leg. What can vary is the muscle development stage, which is explained by the various habits the spiders have - spiders who need to keep down struggling pray have more developed muscles than those who wrap it in a web.

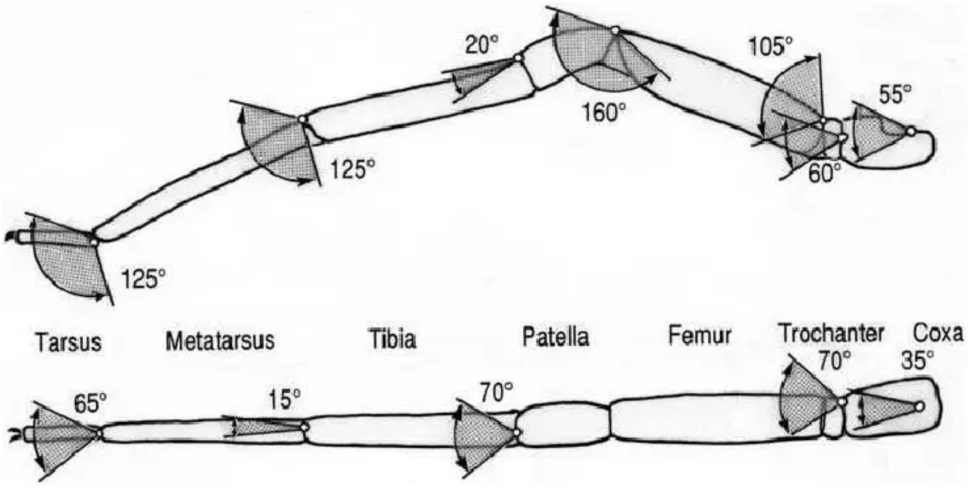

FIGURE 1.2: Spider leg links and movement range as measured on a live wandering spider *Cupiennius* [4].

Most spider joints [4] use either conventional antagonistic actuation with muscles or are tendon-driven. Interestingly, the two most important joints - tibia-metatarsus and femur-patella - are with a dual-actuation mechanism. Instead of using antagonistic muscles for extension and flexion, only flexion muscles exist in these joints. Extension is achieved with hydraulic pressure created in the prosoma of the spider with muscle contraction. Haemolymph - spider's equivalent of blood - is used as the pressure medium, and it flows through the gaps in the muscles called lacunae (see fig 1.3).

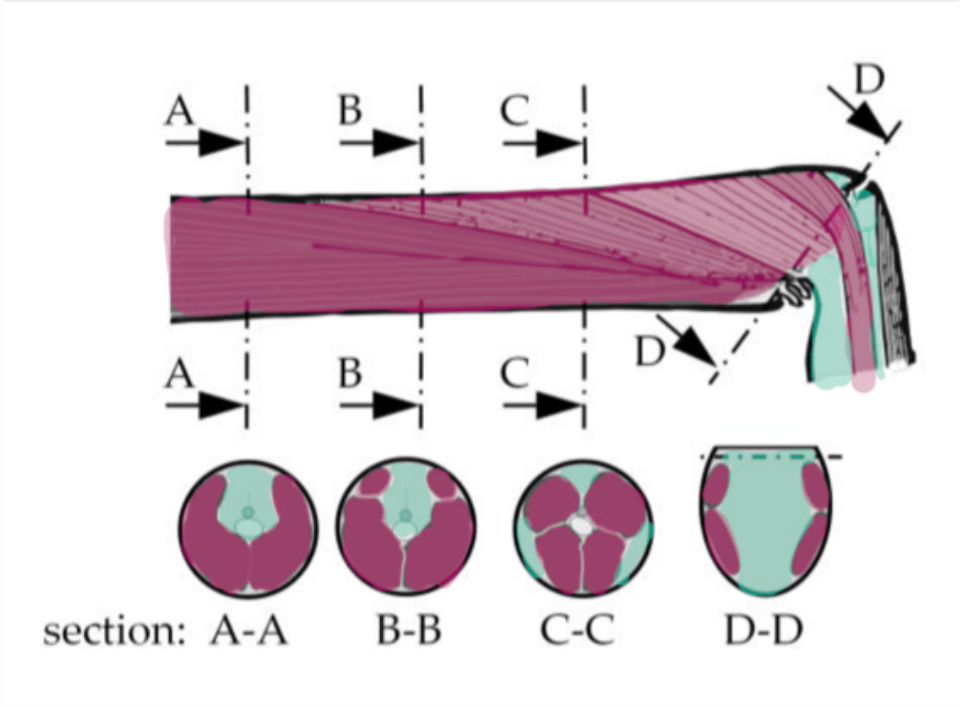

FIGURE 1.3: Spider leg musculature positioning coloured from [9]. Purple - muscle, green - lacunae.

The muscles are attached to a hard external skeleton called the exoskeleton, which protects and supports the soft inner organs and musculature as well as plays an important role in sensing. An exoskeleton is made of cuticle in which various layers with different properties can be distinguished, although the basic components are the same - chitin and various proteins. As seen from figure 1.4 the exoskeleton is thin and soft in the so-called articular membrane (see fig 1.5) to allow for movement of the joints.[4] The articular membrane has not been researched in depth [6]; however, it has been described bellows-like [9, 10] with possible sliding of the folds into each other [6].

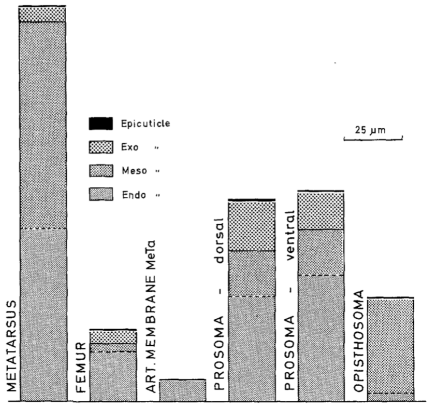

FIGURE 1.4: *Cupiennius salei* cuticle composition at different body locations after a widely used connective tissue visualisation technique Mallory's stain [8]. The composition varies greatly dependent on the function of the body part. Note the thickness and almost singular composition of the articular membrane.

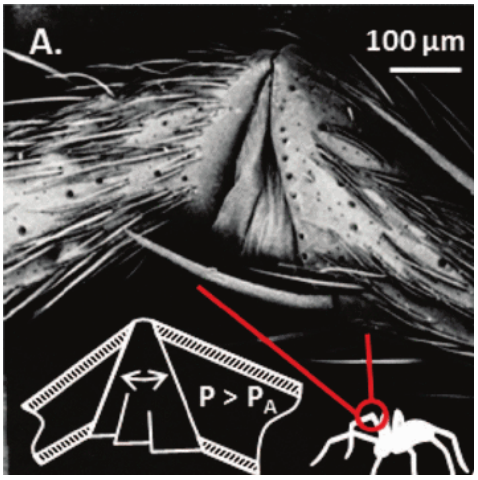

FIGURE 1.5: Articular membrane in the spider leg joint is a thin section of the exoskeleton that allows for the movement of the leg with the bellows-like shape. Image from [11].

What is interesting, it has been experimentally proven that the degree of hydration of the insect exoskeleton protein matrix influences the mechanical properties (stiffness, hardness, toughness and strength)[5] of the exoskeleton to be more flexible when hydrated [12]. The elastic modulus of insect cuticle can cover more than eight orders of magnitude due to variations in cross-linking between the proteins of the matrix, quantity and spatial orientation of crystalline chitin fibres in the matrix, as well as hydration levels [12].

1.1.3 Spider as a model organism for robotics

The spider leg has been an inspiration for robotic applications for 50 years [6] with both the hydraulic actuation mechanism and/or soft bellows-like articular membrane being the main inspiration [6, 11, 13–15]. A thorough overview was written by Landkammer *et al* in 2016 [9] which lists the main works on this topic.

More recent developments in this field have visited the concept of combining an inactive structural part with an active actuating part, for example Han *et al* with light activated nodes intermittent with poly(methyl methacrylate) inactive links [16] and Ma *et al* with pH active muscles embedded on an inactive skeleton [17].

One recent addition by Göttler *et al* in 2021 [6] proves the relevance of the topic as well as the direction of moving closer to the bioinspired design of the joint, not just the functionality as previous work had used the concept of soft bellows. This work is significant due to the fact that it thoroughly focused on characterising the articular membrane, identifying the key aspects such as reinforcing hoops and applying them to the 3D design of hydraulic actuation with improved results over classical bellows with fused deposition modelling 3D printed joints.

The effort to combine electric control with fluids in spider-inspired artificial joints can be seen from the recent work by Kellaris in 2021 *et al* [18]. The electrohydraulic actuators combined the use of electrostatic forces to locally pressurise a hydraulic liquid which resulted in flexion of a segmented structure. The actuation requires high voltage (up to 9 kV), but succeeds in combining the relatively different actuation modes.

Interestingly, one of the first works on spider-inspired joints by Schwörer *et al* [13] was one of the few in similar size scale as spiders with joint size around 1 mm in length. Later works (e.g. the ones described by Landkammer *et al* in 2016 [9]) are larger in scale, mainly from a few to tens of centimetres.

As can be derived, previous work has focused on the dual-actuation of the joint by using the hydraulic mechanism as an inspiration source and/or the compliant bellows to design joints. The incorporation of liquid to change the joint outer shell (exoskeleton) material's elastic properties as hydration levels change the behaviour of arthropod exoskeleton's elastic properties as well as enabling the function of the actuator has not been deeply explored to the author's knowledge.

1.1.4 Artificial Exoskeletons

The spider-inspired joint shells with a continuous structure for liquid or gas containment (for hydraulic of pneumatic actuation) mentioned in the previous chapter have not been usually considered as exoskeletons. It seems that the term "exoskeleton" is mostly used in (human) wearable assisting devices. Artificial exoskeletons of a sort have existed since the beginning of combat - from wearing animal skins to medieval metallic armours to lightweight, modern flexible protective wear [19]. Since at least the early 2000 focused development of exoskeletons in rehabilitation (e.g. neuromuscular impairments [20]) or performance improvement [21] for example occupational tasks [22] has been ongoing.

As for other use cases, such as walking or gripping robots, there have been other solutions. For example, Jiang *et al* [23] developed a new design and fabrication process inspired by insect exoskeletons targeting the sturdiness and flexibility of natural exoskeleton. Their solution, however, was not continuous and resulted in an open structure. Furthermore, work has been done on biohybrid systems to combine muscle tissue with artificial scaffolds in order to replace artificial muscle that cannot compare to native muscles [24].

In this work, the term "exoskeleton" is used in a soft robotic setting to describe an integral part of the actuating joint which protects and encases the liquid and actuator inside.

1.2 Technologies for Milli-scale Robotics

To achieve milli-scale structures, conventional formative and subtractive technologies are used, such as milling, lithography. However, for higher complexity, these technologies may not be sufficient due to low resolution, high cost or technical unfeasibility. To counter this, 3D fabrication can be of use.

1.2.1 3D Microfabrication

The use of additive manufacturing (also known as 3D printing or rapid prototyping) is gaining importance nowadays. The freedom of creating shapes in a computer-aided design (CAD) software and manufacturing the objects in an automatised successive layer-by-layer material deposition makes this a unique method to realise one's imagination. In addition, a wide range of materials is being developed for 3D printing, such as polymers, metals, glasses, composites and active materials.[25] One interesting possibility in biomimicry and bioinspiration is the potential to 3D scan the model organism or structure and subsequently (with possible editions) create an artificial replica.[26]

3D printing is especially attractive for microrobotics due to the possibility of anticipated robot printing to order similar to printed circuit boards. In a recently published review [25], one of the most important technologies for microscale robotics is considered to be laser-based 3D printing (especially direct laser writing DLW).

Direct Laser Writing

In DLW [27–29] the femtosecond (fs) laser is used to photopolymerise a photopolymerisable resin with high precision by using the two photon polymerisation (2PP or TPP) technique which is based on the two photon absorption (TPA) principle. This method requires neither masking nor iterative processes. TPA is an optical non-linearity in which the photo-excitation of a single atom/molecule is caused by multiple photons. This requires high photon density, which induces the simultaneous or sequential absorption of the photons by an electron, resulting in an excited state of the atom/molecule. With a high numerical aperture, it is possible to focus the laser beam so that the TPA induced photopolymerisation is realised in a very small volume where the laser intensity is higher than the TPA threshold (so-called voxel, the 3D analogue of the 2D pixel, see figure 1.6). This is why it is possible to achieve voxel sizes below the used laser's wavelength to sizes below 100 nm. High laser pulse rates reduce the probability of autopolymerisation induced by thermal effects as the photon energy is released faster than the electrons could pass on.

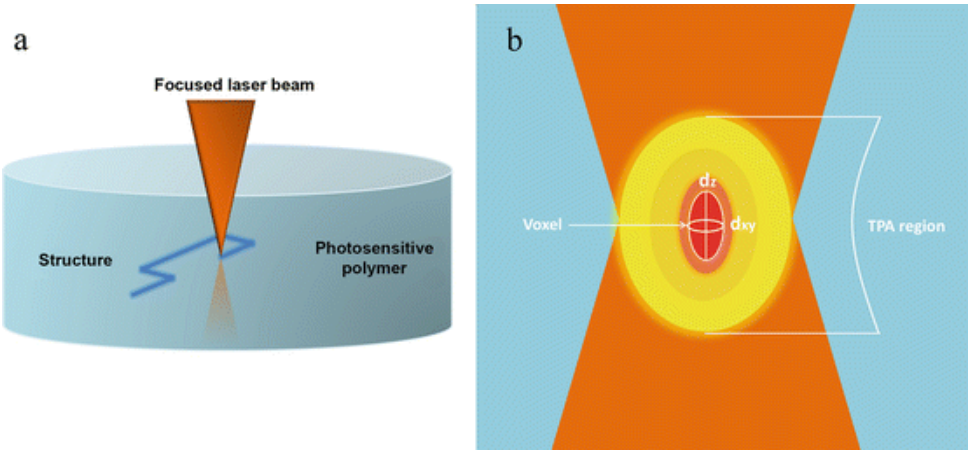

FIGURE 1.6: Working principle of 2PP. a) Focused laser beam will polymerise a photosensitive polymer only where the laser intensity is higher than TPA threshold by user-determined structure. b) Voxel is the photopolymerised area in which the laser intensity is highest. Voxel size is used to describe the resolution of the 3D structure. [28]

The photosensitive materials used for 2PP consist of photoinitiators, monomers/oligomers, crosslinkers, photosensitisers, quenchers and solvents for dilution. The range of available

photoresists is wide and continuously expanding as interest in this field is increasing. Various functional photoresists are being developed for various applications such as biomedical engineering, MEMS and actuators. One option for actuation would be to print intrinsically functional resists (e.g. butylmethacrylate and propoxylated trimethylolpropane triacrylate used by Tian et al for a micromachine actuated by solvent induced swelling [30]) but rational design and tailored operating conditions with commercial resists can also be utilised for a good performance [29].

2PP has been used extensively for microrobotics [17, 31–36]. One perspective field of application for these microrobots has been considered to be biomedical, namely minimally invasive surgery, drug delivery, biopsy and diagnosis [32]. Various driving methods have been studied and exploited, e.g. magnetic force, optical tweezer, acoustic wave, electrostatic force, hydraulic force and stimuli-responsive materials [31]. Creating soft structures with 2PP is can be realised by printing moulds for casting or printing intrinsically soft materials [29].

1.2.2 Artificial Muscles

All moving systems need something to induce the movement - an actuator. Conventional solutions include robust hydraulic or pneumatic systems, electric or fuel engines *et cetera*, but with increased automation and need for safe human-robot interaction, soft robotics, and compliant actuators [37] have gained importance. The field of compliant actuators is wide, and several review articles have focused on the materials and technologies used in soft robotics, [37–40] to name a few, as are focused reviews of actuators for small-scale use (nanometre to centimetre [41]).

One class of materials also used in small scale robotics is ionic electroactive polymers (iEAP) [41] and of , conductive polymers (CPs) represent a class of materials with shape change induced by electric charge due to the mobility and diffusion of ions [41, 42]. The doping of conjugated polymers by adding or detaching electrons to the polymer backbone increases their conductivity [41] and enables actuation via oxidising or reducing the polymer chains, which results in volume change. CPs have low driving voltages up to 3 V, are typically lightweight, flexible, have negligible self-discharge and are feasible to manufacture in the micro-and nanoscale [41]. The actuation process, however, is dependent on the mobility of the ions and thus by material thickness, and requires an ion

source (e.g. electrolyte solution environment) [43] (see fig 1.7 for actuation reference). Some of the most used CPs include poly(3,4-ethylenedioxythiophene) (PEDOT) [44], polyaniline (PANI) and polypyrrole (PPy) [41].

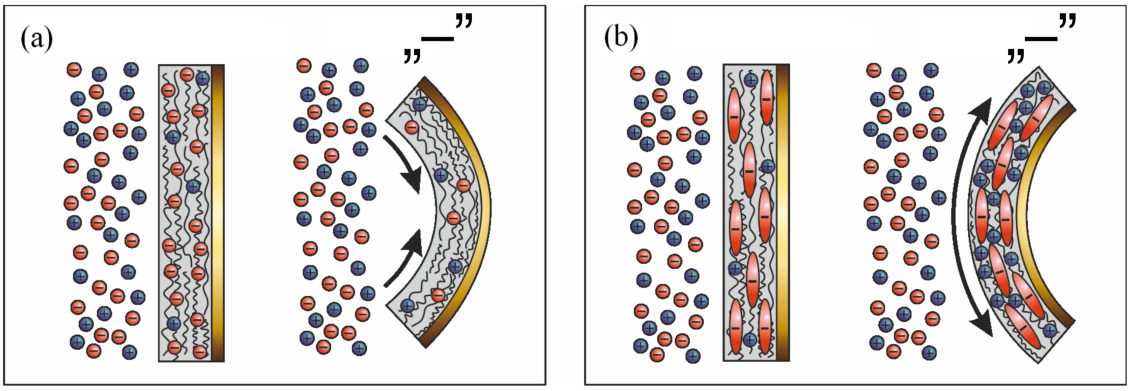

FIGURE 1.7: CV actuation of bending actuators. Anion active CP volume decreases with applied negative potential (a), cation active CP volume increases with applied positive potential (b). Adjusted from [44]

A single piece of CP can act as an actuator as the volume change is the intrinsic material property. To increase the performance (strain, angular change etc) of the actuator, various configurations can be used for different motions, e.g. bulk, linear, bending or out of plane [42]. For linear movement, freestanding films, strips, fibres [42] and tubes [45] can be used. The hollow fibres of PPy(DBS) have shown to achieve larger strain and faster actuation compared to thin film, possibly due to the fact that expansion in the radial direction is converted to the axial direction [42, 45].

PPy is common as a CP actuator due to its low monomer price, stability in oxidised form, high conductivity, and biocompatibility [46]. The preferred synthesis method for high conductivity and actuator application is electrochemical polymerisation as the electric control gives more control over the synthesis product, yield is close to 100% and the deposition of the PPy is on the electrode surface [46]. Synthesis parameters (e.g. temperature, species concentrations, electrolyte, solvent, current/voltage value and application method, additives such as plasticisers, electrodes etc) can be varied to achieve desired PPy properties [47]. Naturally, all the synthesis cell materials must be corrosion resistant in the chosen voltage range and chemicals.

IMS lab experience shows that low temperatures are optimal for PPy electrochemical synthesis for actuator applications as well as galvanostatic (constant current) synthesis with current density of 0.1 $\mathrm{mA\,cm^{-2}}$ [48–50]. Synthesis from 1:1 v/v water and ethylene glycol (EG) solution and actuation in propylene carbonate (PC) solution have given higher performance of PPy-LiTFSI-PEO (lithium bis(trifluoromethanesuflonyl)imide) actuators in regards to strain, stress and charge-efficiency [51]. PEO (poly(ethylene oxide)) has been shown to increase both electrical and mechanical properties of PPy [51].

The mechanical properties of PPy have been known to be highly dependent on synthesis and actuation conditions, causing trouble PPy performance and mechanical properties have been shown to change at different potentials [52] as well as due to synthesis parameters e.g. electrolyte [52], and electrolyte concentration [53]. What is more, the driving ion can change due to mechanical loading as well as change of solvent [54]. It is essential to know the mobile species and establish an as pure as possible cation or anion driven system in order to achieve control over the actuator [55].

1.2.3 Model Based Design and Simulations

Modelling and simulations are widely used in engineering as the underlying mathematical models of materials, and system dynamics have been proven in many real-life applications [56]. A model is here [56] defined as a set of mathematical equations to describe a physical system along with the computational expression of these equations. A simulation is the result of using the model to study a specific motion or event, e.g. to analyse the the motion resulting from the application of forces (dynamic simulation). In addition to geometric systems like musculoskeletal systems, [56], simulations can be used to study ecosystem-scale changes such as the invasion and emergence of forest pests and pathogens [57], or small scale systems such as living cells [58]. Furthermore, simulations can be aligned with experimental data to determine system (e.g. material properties like cohesive strength and fracture energy [59]) properties by calibrating the property of interest until the simulation results match the experimental results.

Biomechanical modelling of motion, especially human mobility [56, 60], is extensively researched to understand the fundamental principles as well as designing assistive devices and planning rehabilitation [56]. What is more, the understanding of the joint mechanisms is important to design bio-inspired mechanical joints, e.g. by the example of human or

animal limbs [60]. Animal exoskeleton modelling has been considered to be a potential source of inspiration for new robotic solutions as well as biological system analysis and understanding [61]. For example, Rajabi *et al* [62] researched the stiff but compliant antennae of stick insects with a combination of biomechanical experiments and numerical modelling. The most substantial influence on the static biomechanical behaviour of the antennae was found to be the tapered shape via modelling. This vital feature highlighting simplifies the complex system and can be used as a basis for the mechanical design of biomimetic touch sensors.

2 Aim and Approach

2.1 Aim of this Work

This work aims to understand the benefits and critical factors of liquid enabled exoskeletons with internal muscles in mm-scale for robotics implementation. For this, the structural/material and actuation cues from (Araneae) exoskeletons (based on research found in detail in chapter 1.1.2) will be used:

- Deformation enabled by exoskeleton thickness and shape variation
- Same material throughout exoskeleton (as in spiders) (no multi-material printing)
- Actuator, based on volumetric change, inside exoskeleton (as in spiders)

As a result, a liquid enabled active exoskeleton at the mm/sub-mm scale will be created:

- Functional liquid component filling (and protected by) a deformable exoskeleton, potentially allowing for simultaneous actuation/stiffness modulation (based on fluidic/electrolytic effect)
- Focused demonstration of a charge driven, actuated exoskeleton portion: 2PP printed compliant structure (mm/sub-mm scale profiled joint between two links) encasing electrolytically active element (PPy fiber/muscle)
- Experimental characterisation

2.2 General Joint Working Principle

The general joint working principle is based on combining a passive exoskeleton with an active internal artificial muscle as in spiders. The linear elongation and compression will

actuate the exoskeleton resulting in movement of the joint (see fig 2.1. More specifically, the muscle is designed to work to compression so that the pulling force applied on the exoskeleton due to the compression of the muscle will result in a change from the neutral state of the joint into the actuated one.

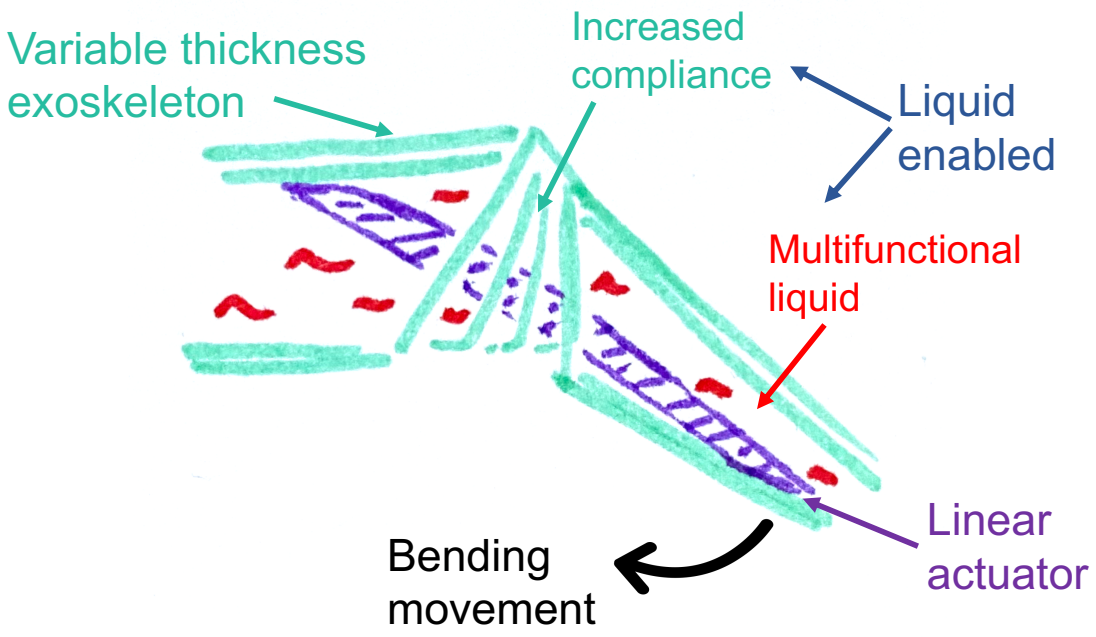

FIGURE 2.1: The joint working principle.

For the artificial muscle, an electrochemically synthesised polypyrrole (PPy) tube will be used. The tube shape will ensure the linear actuation of the muscle as the shape will limit bending in unwanted directions. The properties of the PPy muscle will be characterised to design the exoskeleton.

Two photon polymerisation (2PP) will be used for the exoskeleton fabrication to ensure high resolution structure in the mm to sub-mm scale. The properties of solvent hydrated 2PP structure will be studied, and based on this and the properties of the PPy tube, the simulation-aided design of the exoskeleton will be done.

The liquid used in this study is 0.2 M LITFSI in propylene carbonate (PC) due to its known use in PPy actuators as an electrolyte [49, 51, 55], the low vapour pressure of PC and ability to affect the 2PP photoresist IP-Q (unpublished work).

3 Methods

3.1 Workflow

The methods used in this work are from different fields of research and not commonly used together. In addition to this, the activities are dependent on the results as the results of some methods provide the input to others. The overall workflow is as follows (see fig 3.1):

1. PPy synthesis, mechanical and electrochemical properties characterisation
2. PC immersed IP-Q photoresist effective elastic modulus determination
3. Simulation aided design of the exoskeleton with parameters gathered from points 1 and 2
4. In parallel with 3, testing of the PPy attachment and designing the joint actuation system
5. Characterisation of the joint

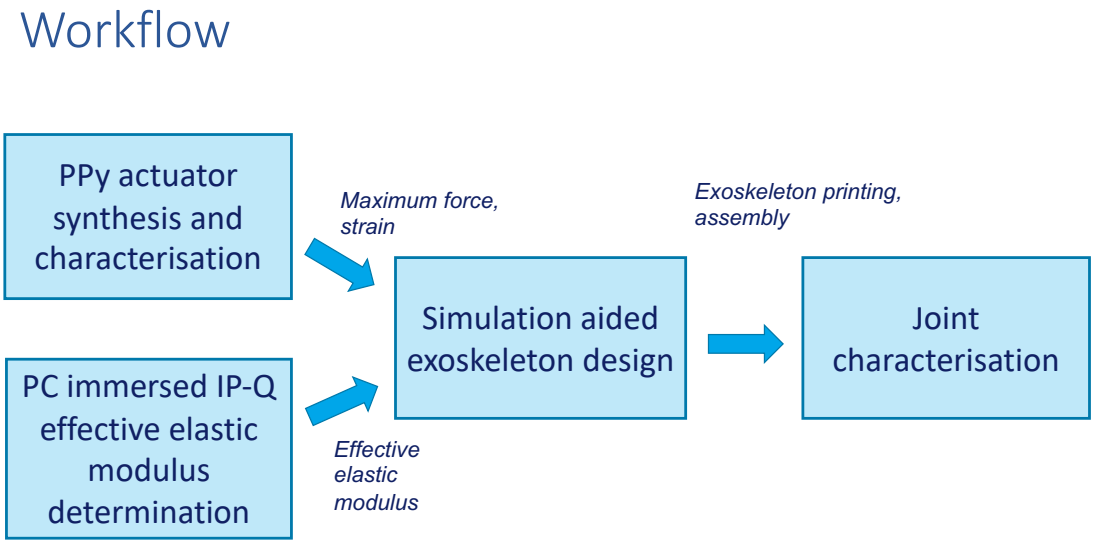

FIGURE 3.1: The workflow of the thesis.

This thesis is a part of an international collaboration between the Italian Institute of Technology (IIT) and the Intelligent Materials and Systems (IMS) laboratory (UT). PPy synthesis and characterisation are in the research field of IMS. The author received guidance from her supervisors Indrek Must, PhD and Tarmo Tamm, PhD, and other IMS colleagues. Two photon polymerisation with Nanoscribe was done with Isabella Fiorello (IIT), and the simulations for the effective elastic modulus of PC immersed IP-Q, and joint design were created with Edoardo Sinibaldi, PhD (IIT).

3.2 Materials

The chemicals used in this study were as follows: pyrrole (Py) from Aldrich (101527050) was distilled and kept at -18 °C. 99.9 % lithium bis(trifluoromethanesuflonyl)imide (LiTFSI) was obtained from Solvionic (S001A250). Polyethylene oxide (PEO) with average molar weight of 100000 $g\,mol^{-1}$ was obtained from Alfa Aesar (42236). Ethylene glycole

(EG; 99% reagent grade) was obtained from Sigma-Aldrich (102466M). MilliQ and milliρ deionised water was used for synthesis and cleaning along with analytic isopropanol, ethanol and acetone. IP-Q photoresist was used with silicon substrates 3D LF DiLL+, both from Nanoscribe GmbH.

Platinum (99.9 %) wire with a diameter of 0.3 mm was obtained from Alfa Aesar (43014). Stainless steel mesh was used as a counter electrode for electrochemical cleaning and synthesis. The reference electrodes used are Ag/AgCl 3 M KCl.

3.3 Exoskeleton Design and Simulation Parameters

The joint model-based design was based on the material and actuation cues from spiders: the deformation enabled by exoskeleton thickness and shape variation, same material throughout the exoskeleton and actuator inside the exoskeleton. The general layout of the joint involves two straight links working as the rigid part of the spider exoskeleton and a compliant bellows between the links functioning as the spider articular membrane (see fig 3.2). COMSOL Multiphysics 5.5 was used for the model build and simulations. The variation of selected parameters altered the geometry of the joint, whereas some geometrical constraints were set due to the physical capabilities of the system (described below).

The material properties - effective elastic modulus of IP-Q photoresist in PC (determined in this work), Poisson's ratio (NanoScribe) and density of polymerised IP-Q photoresist [63] - were not varied. Maximum force was derived from the PPy force measurements (see chapter 3.5.1 for measurement method and chapter 4.1.1 for results) and effective elastic modulus of IP-Q photoresist in PC was determined with numerical-experimental method (see chapter 3.5.2 for measurement method and chapter 4.1.2.1 for results).

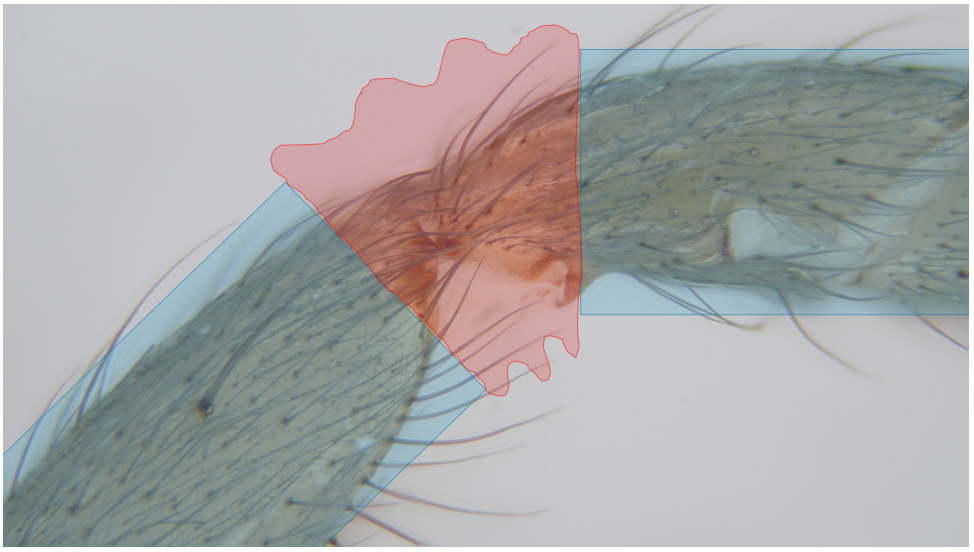

FIGURE 3.2: Rigid links (blue) and compliant bellows (red) are derived from the general structure of the spider leg. Spider exoskeleton was captured by the author.

The maximum overall joint measurements were limited by the maximum printing area of the Nanoscribe machine (maximum height 8 mm) and 10x objective (minimum wall thickness of 20 µm). The compliance of the overall joint is defined by the section connecting the rigid links as this is the region where bending should happen. Furthermore, this should still allow for the containment of all functional elements and withstand torque (future work). Firstly, the wall thickness of the bellows should be as thin as possible yet still preserve a self-supporting property. This is limited by the XY-resolution of the Nanoscribe 10x objective, which is 20 µm at the very least. In order to leave room for possible errors and ease of printing, the minimum wall thickness was chosen to be 30 µm. The wall thickness of the rigid links (100 µm) was decided to be several times the thickness of the compliant part to imitate the spider exoskeleton thickness variation (see fig 3.3). The minimum inner diameter of the joint is 0.6 mm defined by the Pt wire (diameter 0.3 mm) used in PPy synthesis with an approximate diameter ratio of 2:1 estimated to be sufficient to leave room for ion movement necessary for PPy actuation. A joint base was added to fix the joint to the testing setup.

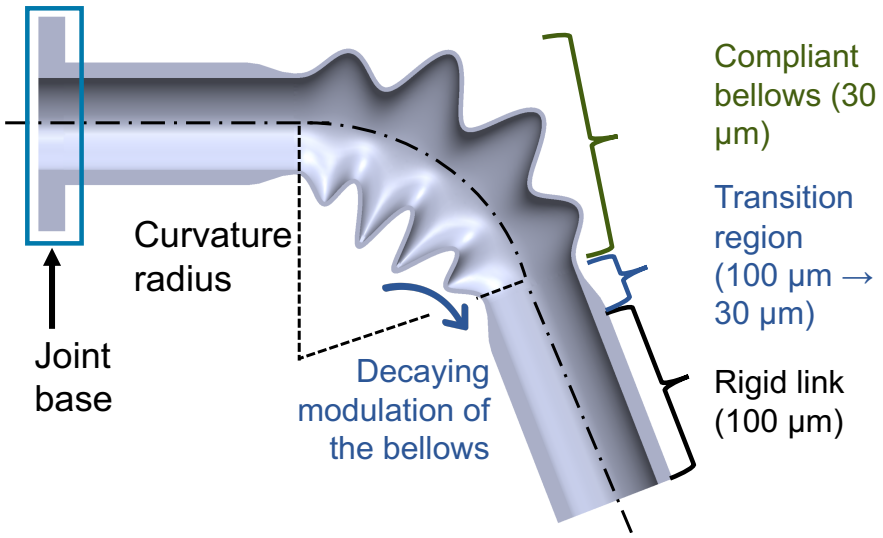

FIGURE 3.3: The cross-section of the model.

The PPy artificial muscle is difficult to simulate due to the shape and positioning. As the PPy muscle is aimed to work with contraction and elongation, it is difficult to know the interaction between the muscle and the exoskeleton, e.g. contact with bellows. That is why a working assumption that the PPy pulling force for the actuation of the exoskeleton represented by a tip force is sufficient to describe the situation. The force was simulated with an added cap on the distal end of the joint. The force was simulated perpendicular to the lower cap area (see appendix 1 for the figure). The optimal fit of the parameters was exported as an STL file, and a base was added with Solidworks 2019-2020 to the dorsal end for the joint fixation to the characterisation setup.

The main area of adjustment was the compliant region with the bellows as the number and shape of the bellows would define the compliance of the system (see fig 3.4. The number of bellows (N_b) would increase the compliance up to a point where the bellows would become too steep and the variation too sharp, making the system lose compliance as well as be non-printable. The shape of the sine-based bellows is defined by the height described by the scaling factor α (α_1 in the outer curvature side, α_2 for the inner curvature side and α_3 for the transverse region). The increase of the value of α increases the height of the bellows and can also cause the bellows to be too steep for physical fabrication. The decaying modulation of the bellows was introduced to smooth the transition from compliant bellows to rigid link.

The four parameters were varied one-by-one in the following ranges: N_b - 1 to 5, α_1 - 0 to 1.5, α_2 - 0 to 1.5, α_3 - 0 to 1.5. The optimum was decided based on highest displacement and lowest relative stress.

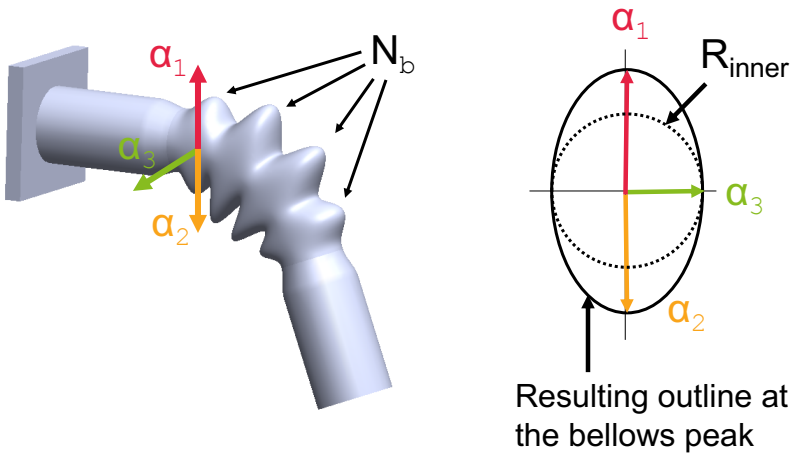

FIGURE 3.4: The parameters varied for this thesis - N_b, α_1, α_2 and α_3. α is a scaling factor that is used to add bellows by defining the increase of radius of the inner tube. In the example, α_3 is zero.

3.4 Fabrication Methods

3.4.1 PPy Synthesis

The fabrication method for the PPy artificial muscle was derived from the knowledge of previous work of the IMS group ([48–51]) for synthesis parameters as well as literature [42, 64] for PPy shape configuration. The tubular shape of the final PPy actuator was chosen as with isotropic volume change the tubular shape will direct the deformation in the longitudinal direction, avoiding unwanted bending as can be the case with thin films/strips (see chapter 1.2.2. PEO was added to increase strain as in [51].

For the manufacture of the artificial muscle, the Pt wire was cleaned electrochemically in 2 M H_2SO_4 by polarising it against stainless steel mesh with "- 1.5 V" and "+ 1.5 V", 10 min for each. Galvanostatic electropolymerisation (PARSTAT 2273) in a two-electrode cell was conducted at temperature -15 °C (Lauda Proline RP 1845 cryostat) with current density of 0.1 mA cm^{-2} for 21200 s on a platinum wire with a stainless steel mesh as the

counter electrode. The synthesis solution consisted of 0.2 M LiTFSI, 0.2 M of Py and 5 w% in a 1:1 MilliQ:EG solution by volume. After synthesis, the PPy thin tubular film on the Pt wire was cleaned with ethanol and deionised water and air-dried for 20 min before positioned into the actuation solution of 0.2 M LiTFSI in PC. PPy was removed from the Pt wire in an HPCL grade acetone bath and returned to the actuation solution.

3.4.2 Exoskeleton and Bellows Fabrication

The printing models were designed in Solidworks 2019-2020 (bellows) or COMSOL Multiphysics 5.5 (joints), and the STL-files were processed for printing in specialised software Describe (slicing distance 5 µm, hatching distance 1 µm, rectangular splitting mode). Nanoscribe Photonic Professional (GT) system (Nanoscribe GmbH) was used to fabricate the exoskeletons. Standard printing parameters for solid 10x silicon wafer substrates were chosen (Toptica laser source with centre wavelength of 780 nm, 90% laser power, scan speed of 50 $\mathrm{mm\,s^{-1}}$ for the base of the structure and 100 $\mathrm{mm\,s^{-1}}$ for the rest of the structure).

Before printing, the silicon substrates were cleaned with a standard procedure of oxygen plasma (Colibrì Plasma RF 50 kHz – Gambetti Kenologia) and attached to the Nanoscribe sample holder with Scotch tape. IP-Q was poured on the substrates and on the 10X immersion objective used for the fabrication. The structures were developed in propylene glycol monomethyl ether acetate (PGMEA, Sigma Aldrich 484431) for 75 min and washed in isopropanol for 75 min and air-dried. The Nanoscribe was operated together with Isabella Fiorello (IIT).

3.5 Characterisation

3.5.1 Actuator

The electrochemical properties were studied using the cyclic voltammetry (CV) technique which is a widely used method [65] to study electrode kinetics. By sweeping the voltage from E1 to E2 to E1 for n times at a scan rate given in units of Volt per second ($\mathrm{V\,s^{-1}}$ or more often $\mathrm{mV\,s^{-1}}$) in an electrolyte solution with electrodes or chemical species under interest, it is possible to interpret based on the resulting current vs voltage graph (voltammogram) what processes are happening. CV is typically done in a three-electrode

cell with the electrode-of-interest working electrode (WE), counter electrode (CE), which is polarised and completes the electric circuit and reference electrode (RE), which is with a known potential and is used to measure the WE potential with more accuracy.

The mechanical properties of polypyrrole were determined to parametrise the design of the exoskeleton. It is important to know the strain and stress the PPy muscle can exert on the exoskeleton. For that, a custom setup was designed, which incorporated a three-electrode electrochemical cell as well as the stress-strain measurement setup (see measurement scheme on fig 3.5 and execution on 3.6). PPy muscle was clamped with gold contact and fixed in a Teflon slit attached to the bottom of the cell. The upper attachment of the PPy muscle was made with Teflon, which was connected to the strain gauge. Custom force sensor based on two strain gauges connected in half-Wheatstone-bridge mode used for the electrochemical measurements was previously described by Must *et al* [66] and for larger force range a commercial force sensor (TRI202PAD, Panlab) with a higher region of measurement was used. The electrochemical cell was attached to a stage with a micro-stage for fixation and pre-straining of the PPy muscle and the main Z-stage to allow static force measurement. For isotonic PPy strain measurement, feedback from the force sensor was relayed to the Z-stage in order to keep the force constant. For blocking force measurement, Z was constant, and force was measured.

Voltage was cycled with scan rate of 10 $\mathrm{mV\,s^{-1}}$) from 0 V to 1 V vs Ag-AgCl (3M KCl) reference electrode in 0.2 M LiTFSI in PC with Ivium CompactStat.h potentiostat. Carbon counter electrode was used. LabVIEW (National Instruments 2020) program (curtesy of Indrek Must) was used to control the stage and record stage displacement, strain gauge and force sensor data.

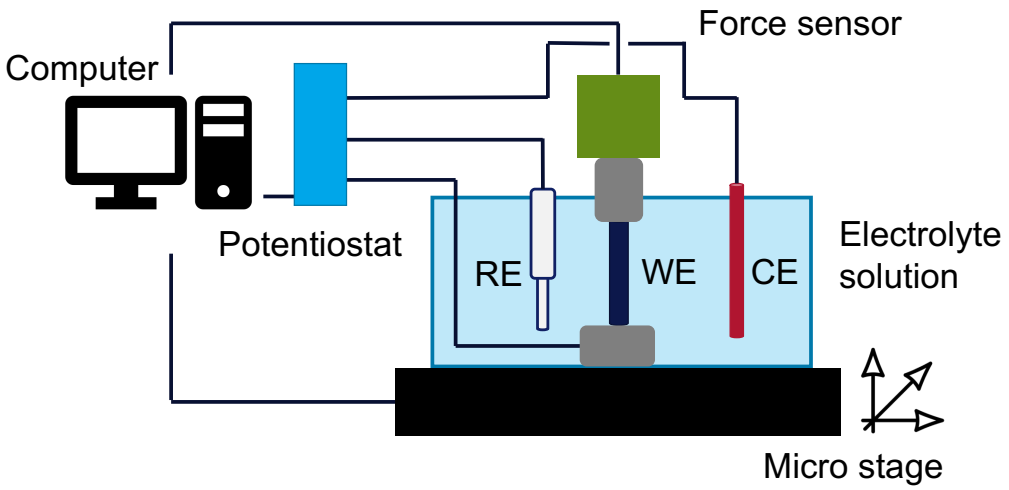

FIGURE 3.5: Experimental setup scheme of PPy characterisation.

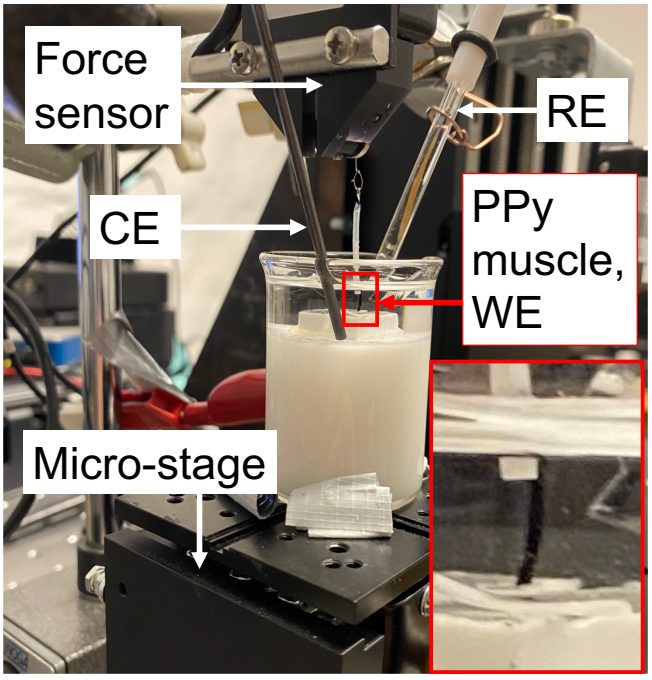

FIGURE 3.6: The electrochemical and electromechanical properties of the PPy muscle were measured in 0.2 M LiTFSI solution in PC in this setup.

3.5.2 Exoskeleton Material Characterisation

To determine the effective elastic modulus of IP-Q immersed in PC, the numerical-experimental method was used. The experimental results were aligned with the numerical via calibration of the elastic modulus until a suitable match between the simulation and the experimental results was found. The Bellows shape (see figs 3.7, 3.8) was used as a sample as the bellows shape was known to be flexible with prior experiments by the author. The structure was immersed for at least 24h before measurements in 0.2 LiTFSI in PC to imitate the conditions used in the joint. The IP-Q structure was placed on an analytical scale in front of a horizontally placed optical microscope(see fig 3.9). The structure was gently compressed multiple times with perpendicular loading to the bellows top surface, and the analytical scale value and video image of the bellows were recorded. Afterwards, the video of loading (force in grams) and compression (compression strain derived with pixel study) were matched in time and data were extracted. The maximum compression strain and force were selected to minimise errors due to inaccurate alignment and value reading.

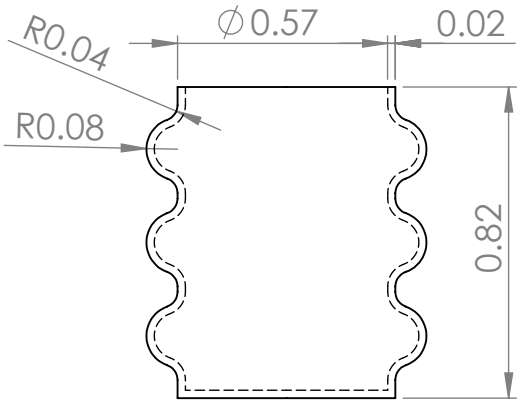

FIGURE 3.7: Side view of the model shape used for effective elastic modulus determination. The original CAD model of the bellows was scaled down in Describe to achieve printing in one piece to avoid attachment errors.

FIGURE 3.8: IP-Q bellows structure used for effective E testing.

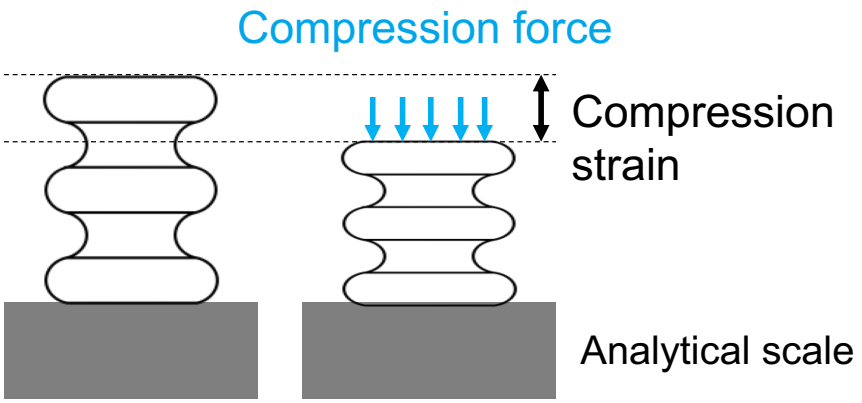

FIGURE 3.9: The PC immersed IP-Q effective elastic modulus determination experimental setup.

The experimental results were aligned with simulations made by Edoardo Sinibaldi, PhD (IIT) in COMSOL Multiphysics 5.5. The simulations used the bellows geometry described in fig 3.7 and material properties such as density (1.2 $\mathrm{g\,cm^{-3}}$ from literature [63]) and the Poisson ratio (0.3 from Nanoscribe website).

3.5.3 Joint Characterisation

For the joint characterisation, the aim was to capture the movement of the joint and to derive the joint tip angle and displacement with image recognition software (LabVIEW 2020 program courtesy of Indrek Must). For the measurements, a setup with a horizontal optical microscope, 3D micro-stage, joint mount, joint, flexible electrolyte vessel, attachment for the PPy muscle and electrodes was designed and assembled (see fig 3.10 for the principal scheme and figs 3.11 and 3.12 for execution). The flexible vessel (thin Teflon sheet) was attached to the 3D micro-stage so that the vessel would allow for the movement of the stage while staying fixed at one end. The joint mount was designed to have a slot for the attachment of the joint and a tunnel for the PPy muscle to move (printed with Nanoscribe). The joint mount was attached on the edge of the flexible vessel and secured to the immobile side of the micro-stage. The PPy muscle was attached to the PC

immersed IP-Q exoskeleton with a piece of fishing line (diameter 0.45 mm, Sufix SFX). The other end of the PPy muscle was attached to the moving part of the micro-stage with a steel plate; electric contact was made with a gold sheet (separated from the steel attachment with Teflon).

A Three-electrode system was used (carbon paper with gold contact as counter electrode and Ag-AgCl 3 M KCl as reference). CV with scan rate of 10 $\mathrm{mV\,s^{-1}}$) from 0 V to 1 V in 0.2 M LiTFSI in PC with Ivium CompactStat.h potentiostat was performed to data about the electrochemical performance of the system. A standard of five to ten cycles was completed.

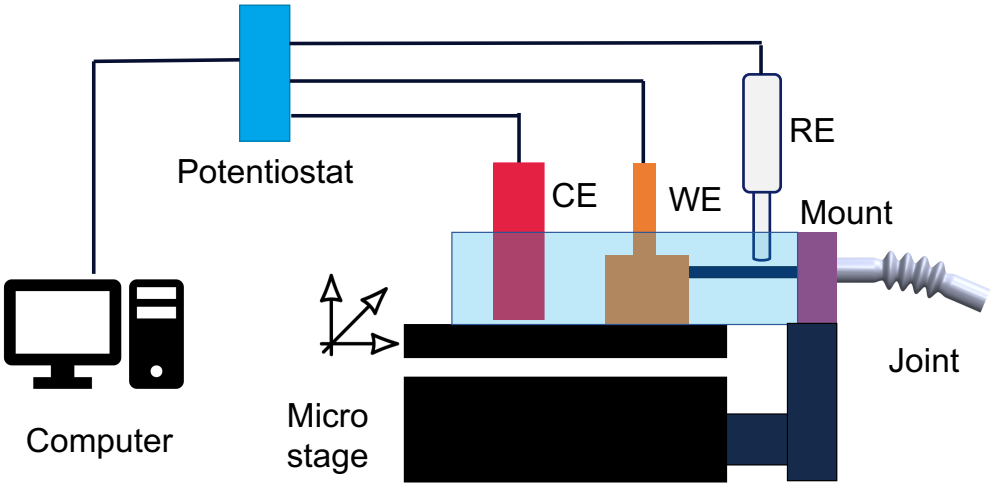

FIGURE 3.10: Experimental setup scheme of joint characterisation.

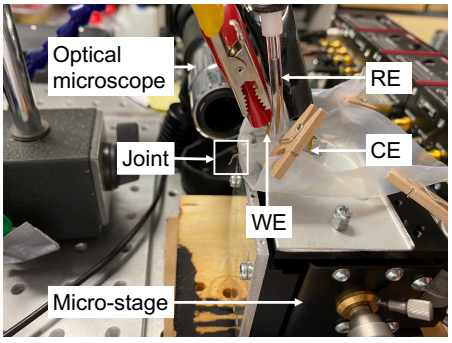

FIGURE 3.11: Experimental setup of the joint characterisation. Front view.

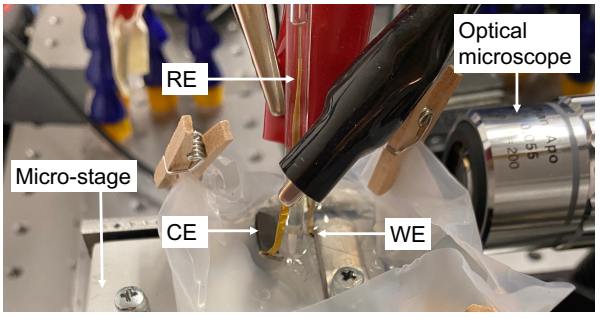

FIGURE 3.12: Experimental setup of the joint characterisation. Side view.

The image recognition software based on the LabVIEW Visual Development module is designed to find in an area of interest the marker (both predetermined by the user, see fig 3.13 for an example) and give out the x and y position in pixels and angle. The area of interest is used to speed up the program by defining the area in which the marker can be found. The marker itself is an area with a characteristic object or part of the object used as a template and fitted to each of the video frames in the area of interest to find the best fit. The marker should be unmistakable, so only the data of the one point of interest is received.

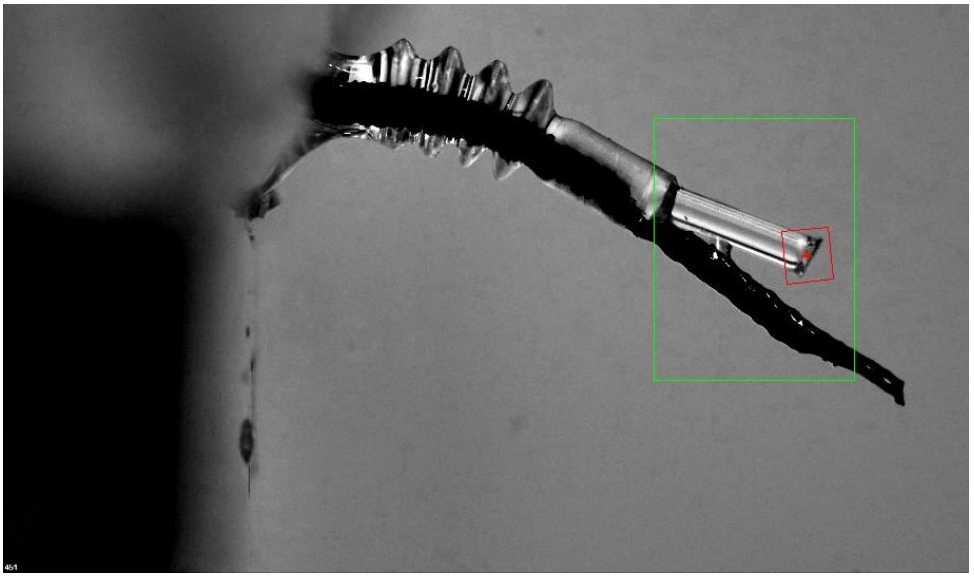

FIGURE 3.13: Angle and displacement determination from actuation video. Area of interest is shown with the green box and selected marker is indicated with the red box.

4 Results and Discussion

4.1 Components

4.1.1 Actuator Performance

The tube-shaped PPy actuator showed desirable electrochemical performance. The rectangular shape of the CV (see fig 4.1) resembles the behaviour of a capacitor. The cycling is repeatable with no apparent irreversible reactions identifiable with current peaks. To characterise the repeatability of the actuation cycle, the positive and negative current densities were summed per cycle, and an average of 91.62 $\mathrm{mA\,cm^{-2}}$ and -91.56 $\mathrm{mA\,cm^{-2}}$ respectively per cycle shows a total of less than 0.1 % inclination towards positive current density. This is a relatively small difference and shows the stability of the actuator in the given potential window. Further stability studies with thousands of cycles were out of the scope of this study.

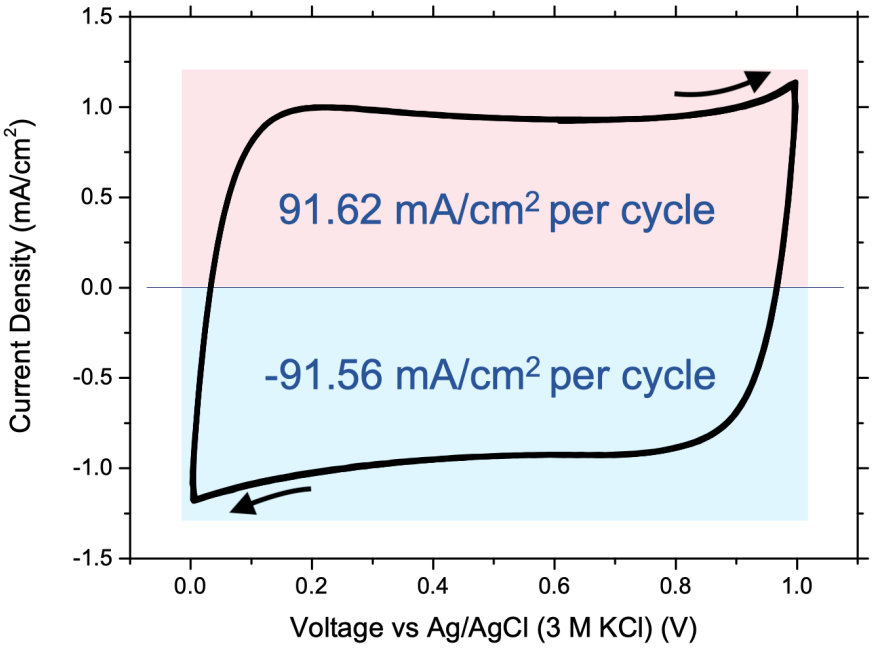

FIGURE 4.1: CV shows excellent capacitor-like behaviour which is desired in actuators. The difference between positive and negative current densities is 0.1 % on average towards positive current density. The PPy muscle was under slight pre-strain (0.1 g).

Furthermore, the strain was calculated from the strain gauge data and aligned with driving voltage data vs time (see fig 4.2). The mobile species in this actuator system is $TFSI^-$ as the strain increases with the voltage, indicating that the anion is moving into the actuator polymer matrix to stabilise the charge and inflicting the volume increase translated into elongation. There seems to be a slight delay (around 30 s) between voltage and strain change in the actuator lengthening region which seems to lessen to around 10-20 s in the discharge region. This could indicate that the insertion of the $TFSI^-$ ions into the PPy matrix is more difficult than the repulsion. This is not consistent with the slight positive difference of 0.1 % towards positive current density as the higher positive current density would indicate ease of oxidation. However, 0.1% is a relatively small difference and does not hold great importance.

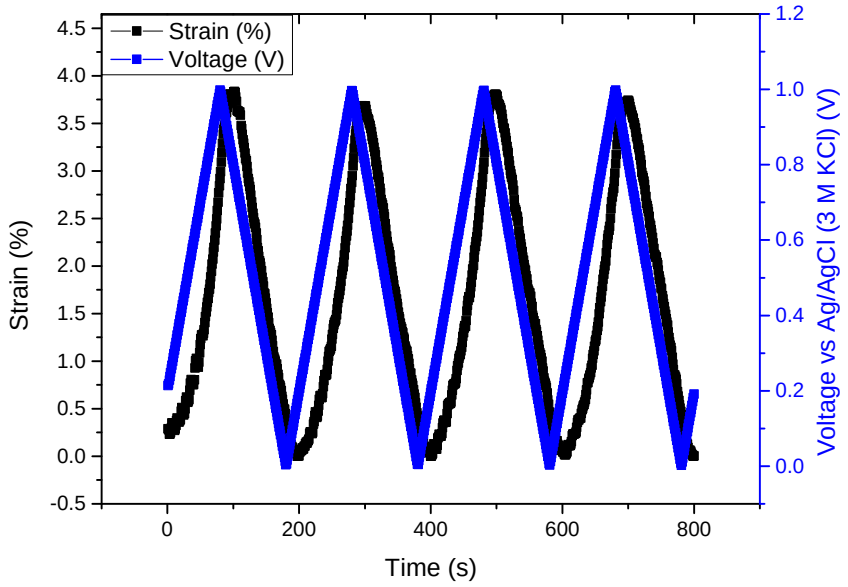

FIGURE 4.2: Strain and voltage vs time of PPy muscle under slight pre-strain (0.1 g) in order to measure strain.

The PPy muscle shortening is designed to actuate the exoskeleton, and elongation of the muscle allows the return of the exoskeleton to the neutral or relaxed state. In order to understand the force with which the PPy muscle is capable of influencing the exoskeleton, the pulling force was measured. The PPy muscle was pre-strained, held at a constant displacement, and a CV was conducted. In fig 4.3 the relative charge applied to the PPy muscle and resulting force can be seen. With the increase of charge, the force is lessened due to the $TFSI^-$ anions moving into the polymer and causing an increase of volume. When discharging, the change is linear until 1.3 g of force with the discharge of one mC resulting in 0.25 g of applied force. The pre-strain of the system may be further increased to achieve a larger force as the PPy muscle is slack in the upper quarter of the applied charge region. However, the force gain to the increased pre-strain may not be proportional as after 1.3 gram-force, the change is not linear anymore.

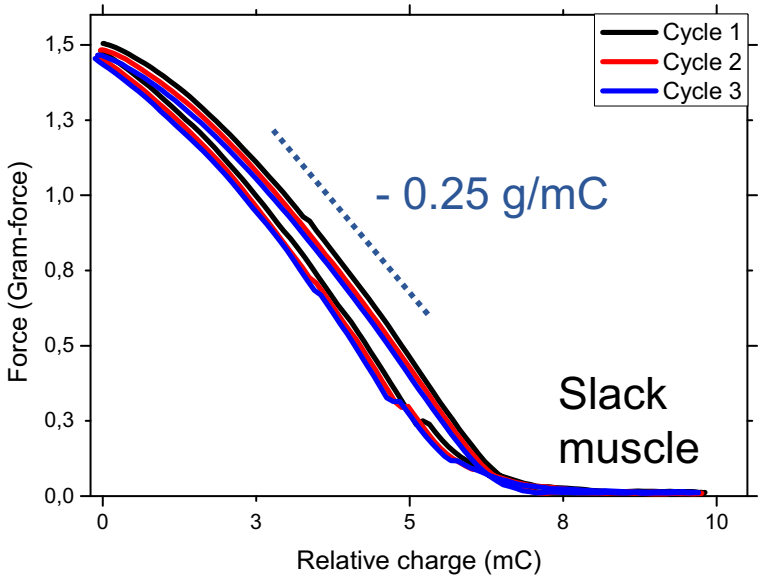

FIGURE 4.3: The relative charge to force relation of pre-strained PPy muscle (1.5 g of pre-strain)

4.1.2 Exoskeleton

4.1.2.1 Properties of the PC Immersed IP-Q

In fig 4.4 the experimental measurements and simulations are aligned in order to determine the best fit for the effective elastic modulus of PC immersed IP-Q. The optimal fit between experimental results and numerical estimation of the tested conditions shows that the effective elastic modulus of the PC immersed IP-Q is in the order of 30 MPa, which is near 150 times less than the dry material property of around 4.5 GPa. The variation of experimental results can be explained as the experimental values were gathered from several compressions of the bellows, not a single compression which could have resulted in slight changes of positions each compression.

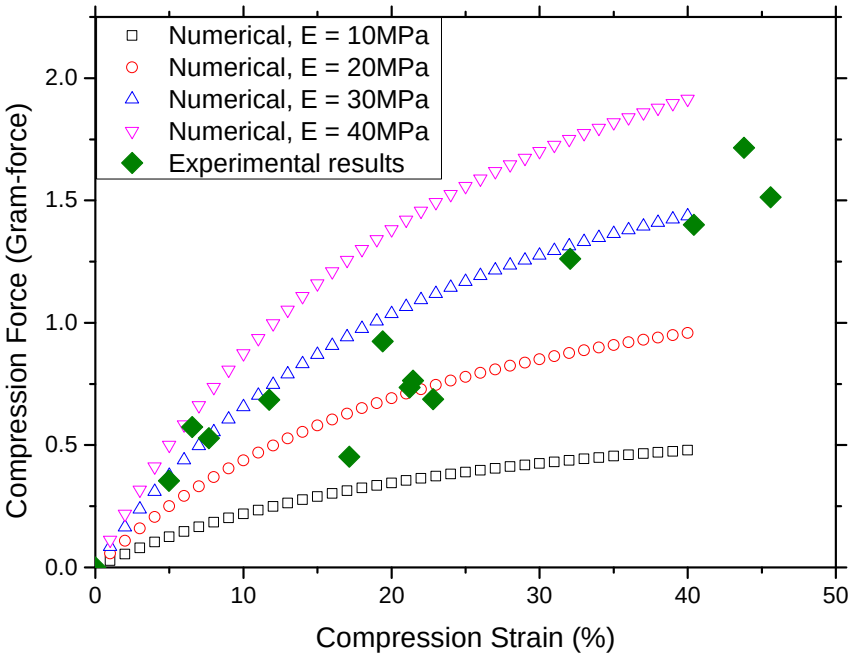

FIGURE 4.4: Experimental immersed structure stress-strain data and simulated materials properties. Seems that the effective elastic modulus of the IP-Q resist immersed in PC for at least 24h is in the order of 30 MPa.

4.1.2.2 Simulation Aided Design of the Exoskeleton

Previous characterisation of the PPy muscle and the PC immersed IP-Q resist had given the required input for simulations - the force that can be applied by the PPy artificial muscle, strain and effective modulus of elasticity of the immersed IP-Q photoresist. Based on these parameters, the models for the joint were built. All the final parameters can be found in appendix 1. These models were designed with Edoardo Sinibaldi, PhD (IIT).

With initial testing of the joint parameters, it became apparent that a slight pre-bending would benefit the system. This would direct the relatively small force applied by the PPy muscle to the exoskeleton into rotational movement. Two types of movements could result with pre-bending - bending movement when force is applied on the tip of a joint with small curvature (see fig. 4.5) and straightening movement if large curvature is used (see fig. 4.7). However, at a certain pre-bending curvature the bending and straightening

movements are nulled and the appliance of force of the magnitude in this study does not have any influence.

The parameters varied in this work were the number of bellows N_b and scaling factors for the bellows in three directions - α_1 in the outer curvature side, α_2 for the inner curvature side and α_3 for the transverse region. The optimum number of bellows was found to be 4, as with four bellows, the exoskeleton had the highest displacement and lowest relative stress. The simulations showed that it is beneficial to have bellows on the outer and inner curvature side. The addition of the perpendicular element (α_3) increased displacement; however, the displacement seemed at times to translate into compression (i.e. shortening of the joint) more than angular rotation, which is the target of this work. To test the activation of the perpendicular element, it was decided to test the all-around bellows (with α_1, α_2 and α_3 activated) for to-bend configuration and opposite bellows (with α_1 and α_2 activated) for to-straighten configuration. The latter showed more similar displacement and stress for activation of both the opposite bellows and all-around compared to the to-bend configuration, which showed clear increased performance for all-around bellows.

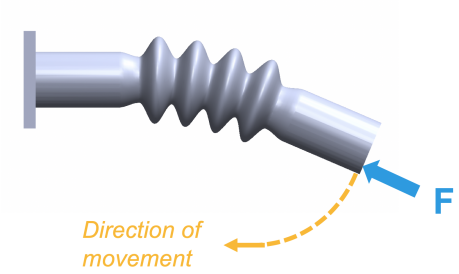

FIGURE 4.5: Working scheme of the to-bend exoskeleton.

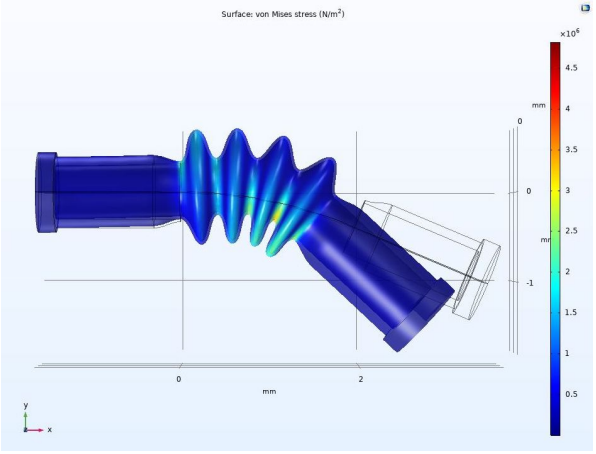

FIGURE 4.6: Simulation result of the to-bend exoskeleton. The lines show the neutral state of the exoskeleton.

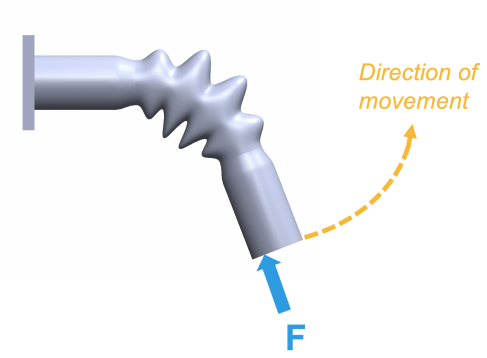

FIGURE 4.7: Working scheme of the to-straighten exoskeleton.

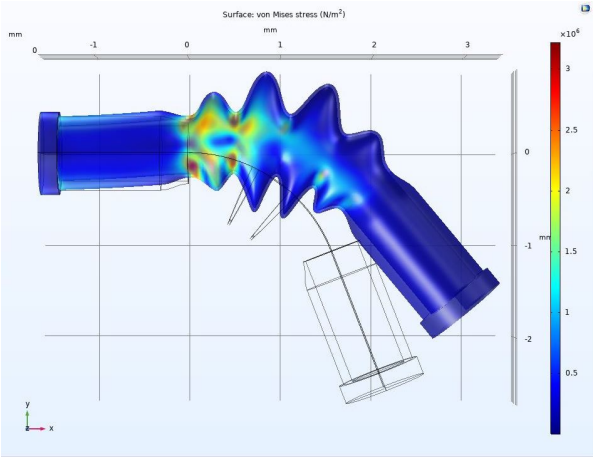

FIGURE 4.8: Simulation result of the to-straighten exoskeleton. The lines show the neutral state of the exoskeleton.

4.2 Joint

4.2.1 Assembly

The assembly of the two configurations of joints had the same basic principle - the joint was conditioned in a 0.2 M LiTFSI in for at least 24h and filled with the electrolyte solution, attached to the characterisation setup, then the PPy muscle was inserted and fixed. On figure 4.9 is a snapshot of the assembled to-bend configuration joint. Note that the PPy muscle, as well as the distal attachment, is visible through the PC immersed exoskeleton. The PPy clamping point is relatively close to the simulated force application site.

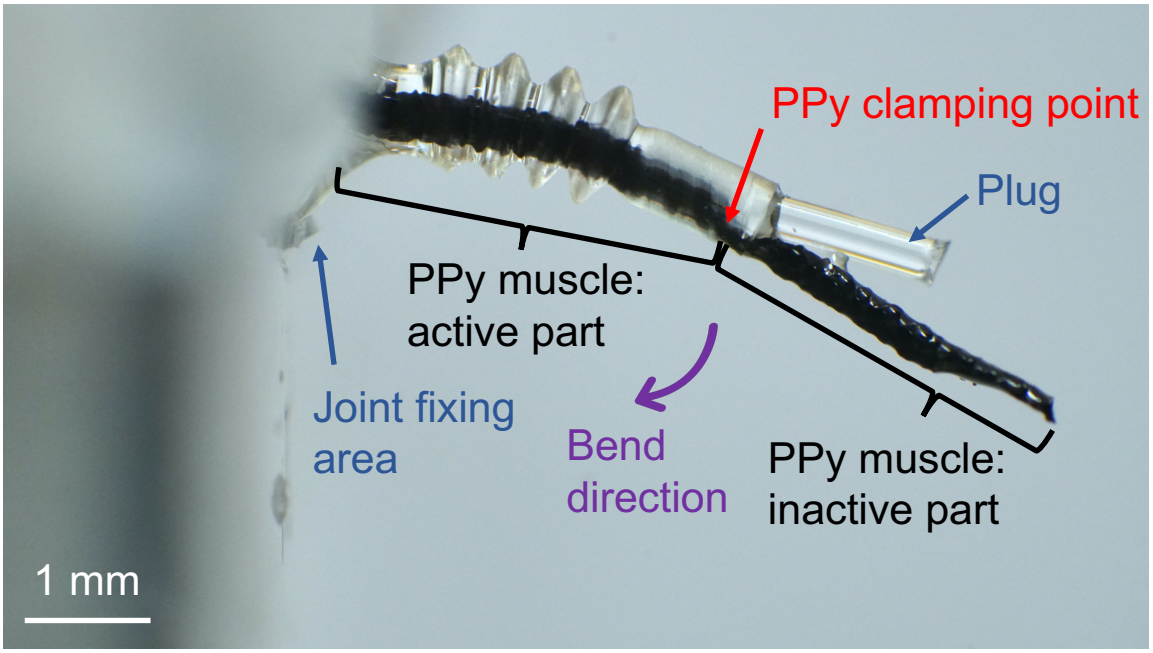

FIGURE 4.9: The assembled to-bend configuration joint. Note that joint is filled with the electrolyte solution and the PPy muscle is visible through the exoskeleton.

4.2.2 Actuation

Experiments show that the actuation of the joint with the cycling of voltage was possible only with to-bend structure. The volumetric change of the PPy visible through the exoskeleton shows how the move is happening.

Maximum angular change visible with a pre-strained system was 15° (see fig 4.10). The angle change of the to-bend structure in time is visible on fig 4.11. In this figure, the angle measurement started from the activated state of the exoskeleton (maximum bending) - the pre-strain applied to the PPy muscle before activating the voltage cycling can be seen on the beginning stage of the actuation. The cyclic amplitude was 5° with a total drift of 3° evident until the third actuation cycle. It could be that the pretension applied to the joint via the pre-strain of PPy muscle is elongating the PPy tube elastically for the short duration before starting the measurement process with voltage cycling. The range of this elongation seems not to be possible to replicate electrochemically, causing a drift as the muscle relaxes into the pre-strained condition while still working. The force applied to the exoskeleton by the PPy can be lower than estimated and with a different vector as estimated (not perfectly perpendicular to the joint end surface). Another opportunity is

that the previously determined effective elastic modulus of the immersed IP-Q is different under these conditions (e.g. joint shape) for unknown reasons.

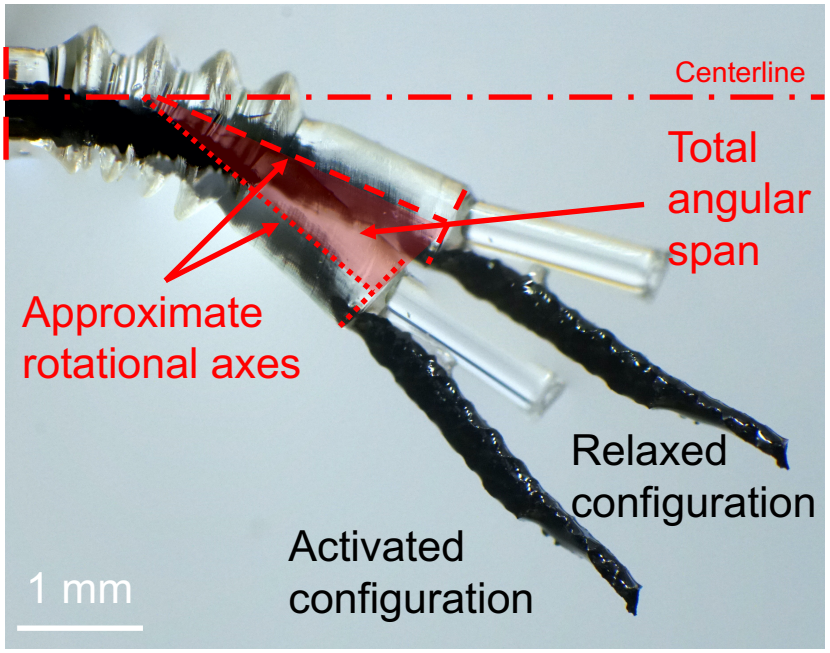

FIGURE 4.10: The neutral state (relaxed configuration) and flexed state (activated configuration) of the to-bend configuration. Maximum angle change of 15° was seen.

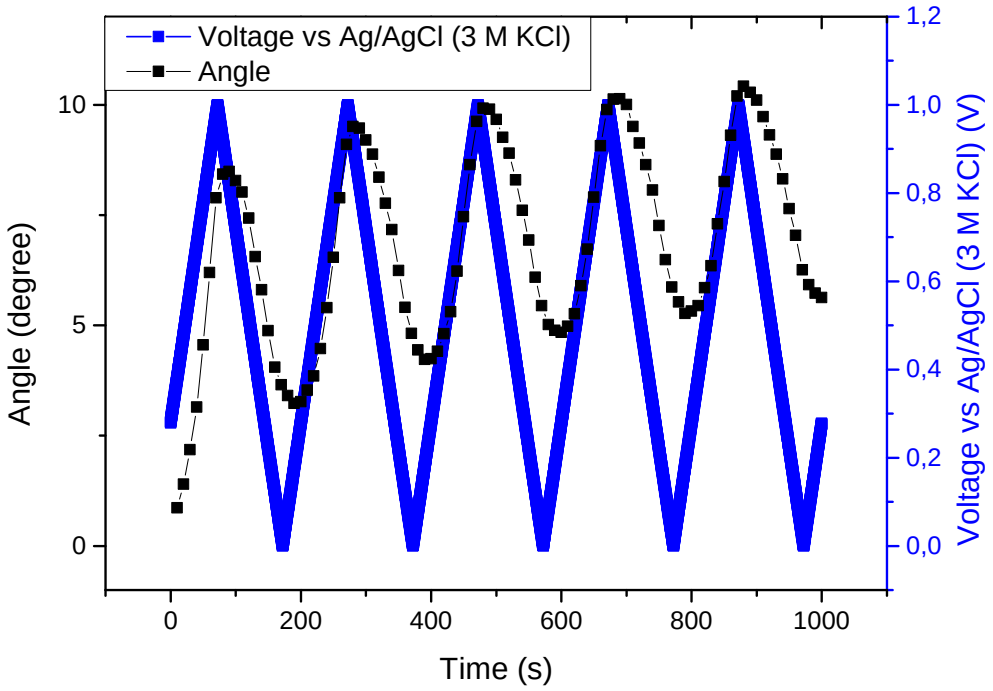

FIGURE 4.11: The actuation angle and the applied voltage of the to-bend configuration.

The to-straighten configuration, however, did not exhibit the simulated deformation. This was possibly due to friction between the PPy muscle and the exoskeleton at the bellows as seen on fig 4.12 which results in an actual fixation point of the PPy muscle in the bend area instead of the joint tip. Even if the friction is negligible, the contact between the exoskeleton and the PPy muscle at the bend would have happened. The fact that the contact resulted in a fixed region of the PPy, was not expected. The slack muscle in the distal link is visible through the distal exoskeleton section as the rest of the muscle is under tension. What is more, the tensioning of the PPy muscle resulted in a barely noticeable bending movement which is opposite the direction designed with the simulations. To conclude, the working assumption of a perpendicular tip load as the PPy muscle in the to-straighten configuration did not describe the physical world adequately. Changing the force application location could benefit the simulations, as well as different positioning of the PPy muscle.

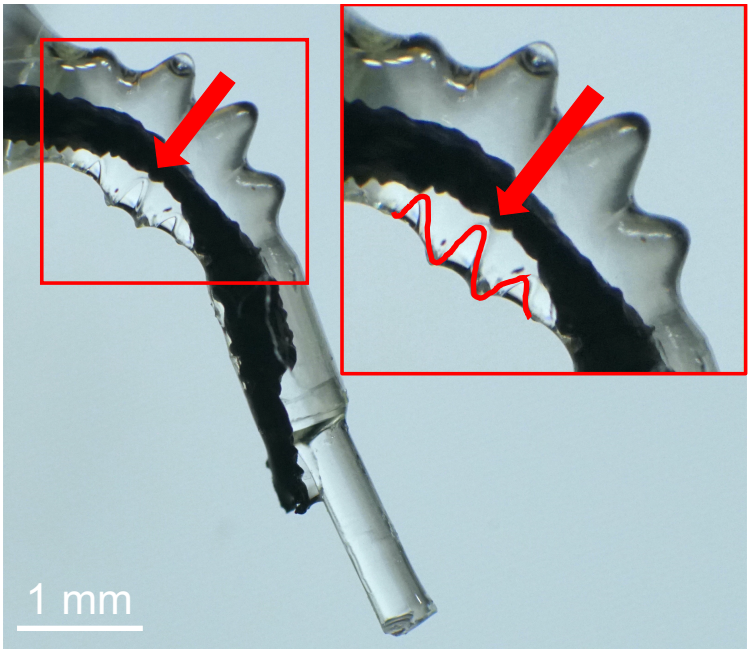

FIGURE 4.12: The to-straighten configuration under PPy tension. The red arrows show the fixation point of PPy muscle due to friction.

The CV of the in joint actuated PPy of both to-bend and to-straighten configurations was compared to the actuation of the PPy tube in the actuation cell - same electric contacts and electrodes as in in-joint CV; however, the electric circuit formation for PPy muscle actuation was not hindered by the compact space in the joint (see fig 4.13). What is good, both the in joint CVs and simply in the actuation flexible vessel tested PPy show similar CV behaviour. The lessened electrochemical performance in the joint can be understood by the fact that the PPy is under mechanical tension with first pretension and afterwards by pulling the exoskeleton as well as the positioning of the electrodes is not optimal. The slight difference between the slopes of early oxidation and reduction can imply that the electric contact was better when the muscle was positioned inside the joint due to better manipulation of the sample.

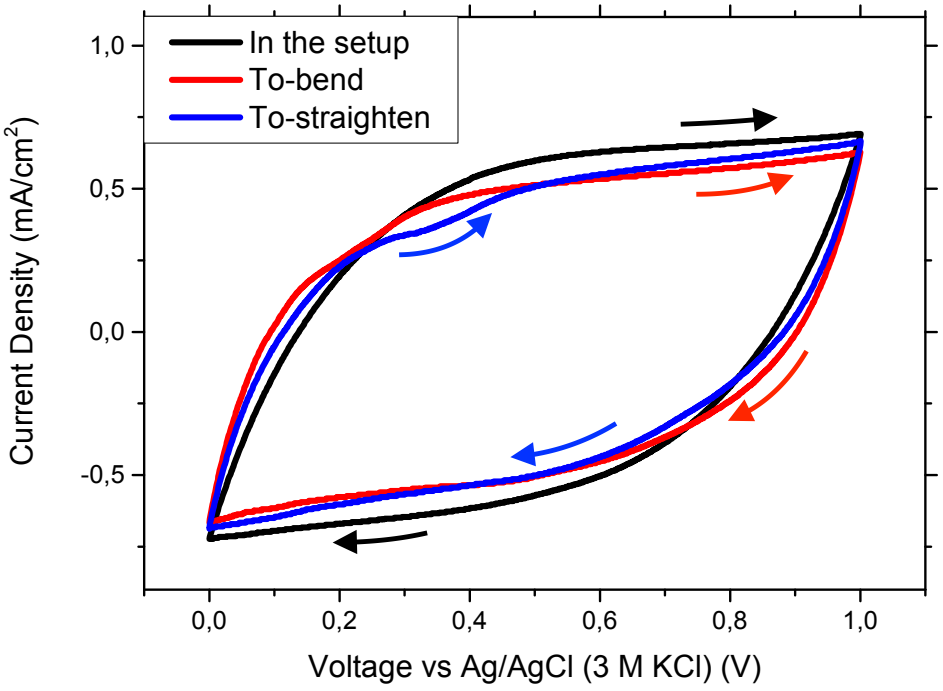

FIGURE 4.13: The CV of The PPy muscle in the joint testing setup - both outside of the joint and in both configurations versions are shown.

4.3 Discussion and Outlook

This work has proven the viability of functional liquid enabled continuous exoskeleton actuation with an internal linear actuator. The joint was enabled by the liquid filling by both allowing for the actuation movement with increased compliance due to immersion resulting in a decrease of effective elastic modulus and actuation functionality of ionic volume change of the PPy muscle induced by electric charge.

In this work, the term "exoskeleton" was used in a mircorobotic application to describe an inactive shell that enabled the movement of the joint. The components of the joint - the exoskeleton, the PPy artificial muscle and functional electrolyte - were integrated to form a harmonious whole. The exoskeleton was as a key component, not as an empowering additive feature as are exoskeletons for human wearable use.

As the bioinspired design is an iterative process [1], the next steps could be to look again at the spider as a model organism with a new understanding gained with this work.

To understand the system better, it could be beneficial to attach the PPy muscle to a force sensor to understand the forces with which the PPy is truly exerting to the exoskeleton as well as fabrication of the working testing setup could be fine-tuned to achieve better electrical contacts, for example. Further simulations could be run to understand and increase the performance of the exoskeleton.

In the further future, the possibility of robotic blood could be researched with a more integrated joint. The addition of hydraulic extension could be integrated into the muscle-based actuation mechanism to study the effectiveness of the biological system. The electrolyte inside the joint could be changed via an artificial bloodstream to provide new chemical species (e.g. pyrrole for the in-situ developing synthesis of the PPy muscle). All in all, an interesting new concept to study.

Conclusion

The performance of functional liquid enabled continuous exoskeleton actuated by internal linear artificial muscle inspired by spiders was studied. For this, the biological model was researched in terms of bioinspiration to determine key aspects to implement in the artificial joint design. To achieve the life-size scale of the joint near to the spider's, microfabrication methods were studied, and complementary technologies 2PP and iEAP PPy were chosen. Two configurations of the joint were researched in-silico based on the resulting movement direction of the joint to the pulling force of the PPy muscle - to-bend and to-straighten. The main parameters varied to increase the compliance of the joint were the number and shape of the bellows.

As a result, in addition to the characterisation of the PPy muscle and PC immersed IP-Q photoresist and simulation-based design, the assemblies of both of the joint configurations were tested. The to-bend configuration showed promise with actuation up to 15° maximum and 5° on average. Performance may be increased with higher PPy muscle pre-strain, improved electrical contacts and reiteration of the bioinspired design process. The to-straighten configuration was inhibited by parameters not possible to simulate - mainly the contact of PPy on the exoskeleton. It was proven that the working assumption of a perpendicular tip load was not descriptive enough for the to-straighten configuration.

All in all, current work introduces a new concept of functional liquid enabled continuous exoskeleton in mm to sub-mm scale. Further work could benefit from detailed joint actuation measurements with a force sensor and higher PPy pretension testing. The future outlook of integrated vascular robotic systems with artificial robotic blood could be foreseen.

Bibliography

[1] Mirko Kovac. The bioinspiration design paradigm: A perspective for soft robotics. *Soft Robotics*, 1(1):28–37, 2014. doi: 10.1089/soro.2013.0004. URL https://www.liebertpub.com/doi/abs/10.1089/soro.2013.0004.

[2] Velcro IP Holdings LLC. About velcro brand. https://www.velcro.com/about-us/our-brand/. Accessed: 20.04.2021.

[3] Peggy Gerullis and Stefan Schuster. Archerfish actively control the hydrodynamics of their jets. *Current Biology*, 24(18):2156–2160, 2014. ISSN 0960-9822. doi: 10.1016/j.cub.2014.07.059. URL https://doi.org/10.1016/j.cub.2014.07.059.

[4] Rainer F. Foelix. *Biology of Spiders*. Oxford University Press, Inc, third edition edition, 2011. URL https://www.academia.edu/13113405/Biology_of_Spiders.

[5] Eoin Parle, Jan-Henning Dirks, and David Taylor. Damage, repair and regeneration in insect cuticle: The story so far, and possibilities for the future. *Arthropod Structure Development*, 46(1):49–55, 2017. ISSN 1467-8039. doi: https://doi.org/10.1016/j.asd.2016.11.008. URL https://www.sciencedirect.com/science/article/pii/S1467803916301931.

[6] Chantal Göttler, Karin Elflein, Roland Siegwart, and Metin Sitti. Spider origami: Folding principle of jumping spider leg joints for bioinspired fluidic actuators. *Advanced Science*, n/a(n/a):2003890, 2021. ISSN 2198-3844. doi: https://doi.org/10.1002/advs.202003890. URL https://onlinelibrary.wiley.com/doi/abs/10.1002/advs.202003890.

[7] D. A. PARRY and R. H. J. BROWN. The hydraulic mechanism of the spider leg. *Journal of Experimental Biology*, 36(2):423–433, 1959. URL https://jeb.biologists.org/content/jexbio/36/2/423.full.pdf.

[8] Friedrich G Barth. Microfiber reinforcement of an arthropod cuticle. *Zeitschrift für Zellforschung und Mikroskopische Anatomie*, 144(3):409–433, 1973. ISSN 0044-3794.

[9] Stefan Landkammer, Florian Winter, Daniel Schneider, and Rüdiger Hornfeck. Biomimetic spider leg joints: a review from biomechanical research to compliant robotic actuators. *Robotics*, 5(3):15, 2016.

[10] Reinhard Blickhan and Friedrich G. Barth. Strains in the exoskeleton of spiders. *Journal of Comparative Physiology A*, 157(1):115–147, 1985. ISSN 1432-1351. doi: 10.1007/BF00611101. URL https://doi.org/10.1007/BF00611101.

[11] A. Spröwitz, C. Göttler, A. Sinha, C. Caer, M. U. Öoztekin, K. Petersen, and M. Sitti. Scalable pneumatic and tendon driven robotic joint inspired by jumping spiders. In *2017 IEEE International Conference on Robotics and Automation (ICRA)*, pages 64–70, 2017. doi: 10.1109/ICRA.2017.7988692.

[12] David Klocke and Helmut Schmitz. Water as a major modulator of the mechanical properties of insect cuticle. *Acta Biomaterialia*, 7(7):2935–2942, 2011. ISSN 1742-7061. doi: https://doi.org/10.1016/j.actbio.2011.04.004. URL https://www.sciencedirect.com/science/article/pii/S1742706111001607.

[13] M. Schwörer, M. Kohl, W. Menz, and V. Saile. Entwicklung fluidischer mikrogelenke. 1998.

[14] Alex Nemiroski, Yanina Y Shevchenko, Adam A Stokes, Baris Unal, Alar Ainla, Sahradha Albert, Gabrielle Compton, Emily MacDonald, Yosyp Schwab, and Caroline Zellhofer. Arthrobots. *Soft robotics*, 4(3):183–190, 2017. ISSN 2169-5172. URL https://www.liebertpub.com/doi/10.1089/soro.2016.0043?url_ver=Z39.88-2003&rfr_id=ori%3Arid%3Acrossref.org&rfr_dat=cr_pub%3Dpubmed&.

[15] Tommaso Ranzani, Sheila Russo, Nicholas W. Bartlett, Michael Wehner, and Robert J. Wood. Increasing the dimensionality of soft microstructures through injection-induced self-folding. *Advanced Materials*, 30(38):1802739, 2018. ISSN 0935-9648. doi: https://doi.org/10.1002/adma.201802739. URL https://onlinelibrary.wiley.com/doi/abs/10.1002/adma.201802739.

[16] Bing Han, Yong-Lai Zhang, Lin Zhu, Ying Li, Zhuo-Chen Ma, Yu-Qing Liu, Xu-Lin Zhang, Xiao-Wen Cao, Qi-Dai Chen, Cheng-Wei Qiu, and Hong-Bo Sun. Plasmonic-assisted graphene oxide artificial muscles. *Advanced Materials*, 31(5):1806386, 2019. ISSN 0935-9648. doi: https://doi.org/10.1002/adma.201806386. URL https://onlinelibrary.wiley.com/doi/abs/10.1002/adma.201806386.

[17] Zhuo-Chen Ma, Yong-Lai Zhang, Bing Han, Xin-Yu Hu, Chun-He Li, Qi-Dai Chen, and Hong-Bo Sun. Femtosecond laser programmed artificial musculoskeletal systems. *Nature Communications*, 11(1):4536, 2020. ISSN 2041-1723. doi: 10.1038/s41467-020-18117-0. URL https://doi.org/10.1038/s41467-020-18117-0https://www.ncbi.nlm.nih.gov/pmc/articles/PMC7484797/pdf/41467_2020_Article_18117.pdf.

[18] Nicholas Kellaris, Philipp Rothemund, Yi Zeng, Shane K. Mitchell, Garrett M. Smith, Kaushik Jayaram, and Christoph Keplinger. Spider-inspired electrohydraulic actuators for fast, soft-actuated joints. *Advanced Science*, n/a(n/a):2100916, 2021. ISSN 2198-3844. doi: https://doi.org/10.1002/advs.202100916. URL https://onlinelibrary.wiley.com/doi/abs/10.1002/advs.202100916.

[19] Zachary W White and Franck J Vernerey. Armours for soft bodies: how far can bioinspiration take us? *Bioinspiration & Biomimetics*, 13(4):041004, may 2018. doi: 10.1088/1748-3190/aababa. URL https://doi.org/10.1088/1748-3190/aababa.

[20] Antonio Rodríguez-Fernández, Joan Lobo-Prat, and Josep M. Font-Llagunes. Systematic review on wearable lower-limb exoskeletons for gait training in neuromuscular impairments. *Journal of NeuroEngineering and Rehabilitation*, 18(1):22, 2021. ISSN 1743-0003. doi: 10.1186/s12984-021-00815-5. URL https://doi.org/10.1186/s12984-021-00815-5.

[21] Gregory S. Sawicki, Owen N. Beck, Inseung Kang, and Aaron J. Young. The exoskeleton expansion: improving walking and running economy. *Journal of NeuroEngineering and Rehabilitation*, 17(1):25, 2020. ISSN 1743-0003. doi: 10.1186/s12984-020-00663-9. URL https://doi.org/10.1186/s12984-020-00663-9.

[22] Mona Bär, Benjamin Steinhilber, Monika A. Rieger, and Tessy Luger. The influence of using exoskeletons during occupational tasks on acute physical stress and strain compared to no exoskeleton – a systematic review and meta-analysis. *Applied Ergonomics*, 94:103385, 2021. ISSN 0003-6870. doi: https://doi.org/10.1016/j.apergo.2021.103385. URL https://www.sciencedirect.com/science/article/pii/S0003687021000326.

[23] Mingsong Jiang, Ziyi Zhou, and Nicholas Gravish. Flexoskeleton printing enables versatile fabrication of hybrid soft and rigid robots. *Soft Robotics*, 7(6):770–778,

2020. doi: 10.1089/soro.2019.0156. URL https://www.liebertpub.com/doi/abs/10.1089/soro.2019.0156.

[24] Maria Guix, Rafael Mestre, Tania Patiño, Marco De Corato, Judith Fuentes, Giulia Zarpellon, and Samuel Sánchez. Biohybrid soft robots with self-stimulating skeletons. *Science Robotics*, 6(53):eabe7577, 2021. doi: 10.1126/scirobotics.abe7577. URL https://robotics.sciencemag.org/content/robotics/6/53/eabe7577.full.pdf.

[25] Jinhua Li and Martin Pumera. 3d printing of functional microrobots. *Chemical Society Reviews*, 50(4):2794–2838, 2021. ISSN 0306-0012. doi: 10.1039/D0CS01062F. URL http://dx.doi.org/10.1039/D0CS01062F.

[26] Chunbao Liu, Shanshi Chen, Chuang Sheng, Peng Ding, Zhihui Qian, and Lei Ren. The art of a hydraulic joint in a spider's leg: modelling, computational fluid dynamics (cfd) simulation, and bio-inspired design. *Journal of Comparative Physiology A*, 205(4):491–504, 2019. ISSN 1432-1351. doi: 10.1007/s00359-019-01336-2. URL https://doi.org/10.1007/s00359-019-01336-2.

[27] Sangmo Koo. Advanced micro-actuator/robot fabrication using ultrafast laser direct writing and its remote control. *Applied Sciences*, 10(23):8563, 2020. ISSN 2076-3417. URL https://www.mdpi.com/2076-3417/10/23/8563.

[28] Anastasia Shpichka, Anastasia Koroleva, Daria Kuznetsova, Vitaliy Burdukovskii, Boris Chichkov, Viktor Bagratashvili, and Peter Timashev. *Two-Photon Polymerization in Tissue Engineering*, pages 71–98. Springer International Publishing, Cham, 2018. ISBN 978-3-319-75801-5. doi: 10.1007/978-3-319-75801-5_3. URL https://doi.org/10.1007/978-3-319-75801-5_3.

[29] Marco Carlotti and Virgilio Mattoli. Functional materials for two-photon polymerization in microfabrication. *Small*, 15(40):1902687, 2019. ISSN 1613-6810. doi: 10.1002/smll.201902687. URL https://onlinelibrary.wiley.com/doi/abs/10.1002/smll.201902687https://onlinelibrary.wiley.com/doi/pdfdirect/10.1002/smll.201902687?download=true.

[30] Y. Tian, Y. L. Zhang, H. Xia, L. Guo, J. F. Ku, Y. He, R. Zhang, B. Z. Xu, Q. D. Chen, and H. B. Sun. Solvent response of polymers for micromachine manipulation. *Phys Chem Chem Phys*, 13(11):4835–8, 2011. ISSN 1463-9076. doi:

10.1039/c0cp02006k. 1463-9084 Tian, Ye Zhang, Yong-Lai Xia, Hong Guo, Li Ku, Jin-Feng He, Yan Zhang, Ran Xu, Bin-Zong Chen, Qi-Dai Sun, Hong-Bo Journal Article England Phys Chem Chem Phys. 2011 Mar 21;13(11):4835-8. doi: 10.1039/c0cp02006k. Epub 2011 Feb 11.

[31] Yang Lin and Jie Xu. Microstructures fabricated by two-photon polymerization and their remote manipulation techniques: Toward 3d printing of micromachines. *Advanced Optical Materials*, 6(8):1701359, 2018. ISSN 2195-1071. doi: https://doi.org/10.1002/adom.201701359. URL `https://onlinelibrary.wiley.com/doi/abs/10.1002/adom.201701359`.

[32] Carlos C. J. Alcântara, Sangwon Kim, Sunkey Lee, Bumjin Jang, Prakash Thakolkaran, Jin-Young Kim, Hongsoo Choi, Bradley J. Nelson, and Salvador Pané. 3d fabrication of fully iron magnetic microrobots. *Small*, 15(16):1805006, 2019. ISSN 1613-6810. doi: https://doi.org/10.1002/smll.201805006. URL `https://onlinelibrary.wiley.com/doi/abs/10.1002/smll.201805006`.

[33] Muhammad A Zeeshan, Roman Grisch, Eva Pellicer, Kartik M Sivaraman, Kathrin E Peyer, Jordi Sort, Berna Özkale, Mahmut S Sakar, Bradley J Nelson, and Salvador Pané. Hybrid helical magnetic microrobots obtained by 3d template-assisted electrodeposition. *Small*, 10(7):1284–1288, 2014. ISSN 1613-6810. URL `https://onlinelibrary.wiley.com/doi/pdfdirect/10.1002/smll.201302856?download=true`.

[34] Mei Dong, Xiaopu Wang, Xiang-Zhong Chen, Fajer Mushtaq, Siyu Deng, Caihong Zhu, Harun Torlakcik, Anastasia Terzopoulou, Xiao-Hua Qin, Xuanzhong Xiao, Josep Puigmartí-Luis, Hongsoo Choi, Ana Paula Pêgo, Qun-Dong Shen, Bradley J. Nelson, and Salvador Pané. 3d-printed soft magnetoelectric microswimmers for delivery and differentiation of neuron-like cells. *Advanced Functional Materials*, 30 (17):1910323, 2020. ISSN 1616-301X. doi: https://doi.org/10.1002/adfm.201910323. URL `https://onlinelibrary.wiley.com/doi/abs/10.1002/adfm.201910323`.

[35] Seungmin Lee, Jin-young Kim, Junyoung Kim, Ali Kafash Hoshiar, Jongeon Park, Sunkey Lee, Jonghyun Kim, Salvador Pané, Bradley J. Nelson, and Hongsoo Choi. A needle-type microrobot for targeted drug delivery by affixing to a microtissue. *Advanced Healthcare Materials*, 9(7):1901697, 2020. ISSN 2192-2640. doi: https://

doi.org/10.1002/adhm.201901697. URL https://onlinelibrary.wiley.com/doi/abs/10.1002/adhm.201901697.

[36] Victor Vieille, Roxane Pétrot, Olivier Stéphan, Guillaume Delattre, Florence Marchi, Marc Verdier, Orphée Cugat, and Thibaut Devillers. Fabrication and magnetic actuation of 3d-microprinted multifunctional hybrid microstructures. *Advanced Materials Technologies*, 5(10):2000535, 2020. ISSN 2365-709X. doi: https://doi.org/10.1002/admt.202000535. URL https://onlinelibrary.wiley.com/doi/abs/10.1002/admt.202000535.

[37] Guanjun Bao, Hui Fang, Lingfeng Chen, Yuehua Wan, Fang Xu, Qinghua Yang, and Libin Zhang. Soft robotics: Academic insights and perspectives through bibliometric analysis. *Soft Robotics*, 5(3):229–241, 2018. doi: 10.1089/soro.2017.0135. URL https://www.liebertpub.com/doi/abs/10.1089/soro.2017.0135https://www.liebertpub.com/doi/pdfplus/10.1089/soro.2017.0135.

[38] Mahdi Ilami, Hosain Bagheri, Reza Ahmed, E. Olga Skowronek, and Hamid Marvi. Materials, actuators, and sensors for soft bioinspired robots. *Advanced Materials*, n/a(n/a):2003139, 2020. ISSN 0935-9648. doi: https://doi.org/10.1002/adma.202003139. URL https://onlinelibrary.wiley.com/doi/abs/10.1002/adma.202003139.

[39] Nazek El-Atab, Rishabh B. Mishra, Fhad Al-Modaf, Lana Joharji, Aljohara A. Alsharif, Haneen Alamoudi, Marlon Diaz, Nadeem Qaiser, and Muhammad Mustafa Hussain. Soft actuators for soft robotic applications: A review. *Advanced Intelligent Systems*, 2(10):2000128, 2020. ISSN 2640-4567. doi: 10.1002/aisy.202000128. URL https://onlinelibrary.wiley.com/doi/abs/10.1002/aisy.202000128https://onlinelibrary.wiley.com/doi/pdfdirect/10.1002/aisy.202000128?download=true.

[40] Joselle M. McCracken, Brian R. Donovan, and Timothy J. White. Materials as machines. *Advanced Materials*, 32(20):1906564, 2020. ISSN 0935-9648. doi: 10.1002/adma.201906564. URL https://onlinelibrary.wiley.com/doi/abs/10.1002/adma.201906564https://onlinelibrary.wiley.com/doi/pdfdirect/10.1002/adma.201906564?download=true.

[41] Lindsey Hines, Kirstin Petersen, Guo Zhan Lum, and Metin Sitti. Soft actuators for small-scale robotics. *Advanced Materials*, 29(13):1603483, 2017. ISSN 0935-9648. doi: 10.1002/adma.201603483. URL `https://onlinelibrary.wiley.com/doi/abs/10.1002/adma.201603483https://onlinelibrary.wiley.com/doi/pdfdirect/10.1002/adma.201603483?download=true`.

[42] Daniel Melling, Jose G. Martinez, and Edwin W. H. Jager. Conjugated polymer actuators and devices: Progress and opportunities. *Advanced Materials*, 31(22): 1808210, 2019. ISSN 0935-9648. doi: https://doi.org/10.1002/adma.201808210. URL `https://onlinelibrary.wiley.com/doi/abs/10.1002/adma.201808210`.

[43] Toribio F. Otero and José G. Martínez. *Conducting Polymers as EAPs: Fundamentals and Materials*, pages 237–255. Springer International Publishing, Cham, 2016. ISBN 978-3-319-31530-0. doi: 10.1007/978-3-319-31530-0_11.

[44] Rauno Temmer. *Electrochemistry and Novel Applications of Chemically Synthesized Conductive Polymer Electrodes*. PhD thesis, University of Tartu, 2014.

[45] Kentaro Yamato and Keiichi Kaneto. Tubular linear actuators using conducting polymer, polypyrrole. *Analytica Chimica Acta*, 568(1):133–137, 2006. ISSN 0003-2670. doi: https://doi.org/10.1016/j.aca.2005.12.030. URL `https://www.sciencedirect.com/science/article/pii/S0003267005020118`.

[46] Tatyana V. Vernitskaya and Oleg N. Efimov. Polypyrrole: a conducting polymer; its synthesis, properties and applications. *Russian Chemical Reviews*, 66(5):443, 1997.

[47] Gordon Wallace, G. M. Spinks, Leon A. P. Kane-Maguire, and Peter R. Teasdale. *Conductive Electroactive Polymers: Intelligent Polymer Systems, Third Edition*. 01 2008. doi: 10.1201/9781420067156.

[48] Rauno Temmer, Indrek Must, Friedrich Kaasik, Alvo Aabloo, and Tarmo Tamm. Combined chemical and electrochemical synthesis methods for metal-free polypyrrole actuators. *Sensors and Actuators B: Chemical*, 166-167:411–418, 2012. ISSN 0925-4005. doi: https://doi.org/10.1016/j.snb.2012.01.075. URL `https://www.sciencedirect.com/science/article/pii/S092540051200233X`.

[49] Tran Thien Khanh, Arko Kesküla, Zane Zondaka, Madis Harjo, Alo Kivilo, Mahdi Safaei Khorram, Tarmo Tamm, and Rudolf Kiefer. Role of polymerization temperature on the performance of polypyrrole/dodecylbenzenesulphonate linear actuators. *Synthetic Metals*, 247:53–58, 2019. ISSN 0379-6779. doi: https://doi.org/10.1016/j.synthmet.2018.11.013. URL https://www.sciencedirect.com/science/article/pii/S0379677918305381.

[50] Kadri-Ann Valdur. Polymer actuators with coil electrodes, 2019.

[51] Roshan Khadka, Peikai Zhang, Ngoc Tuan Nguyen, Tarmo Tamm, Jadranka Travas-Sejdic, Toribio F. Otero, and Rudolf Kiefer. Role of polyethylene oxide content in polypyrrole linear actuators. *Materials Today Communications*, 23:100908, 2020. ISSN 2352-4928. doi: https://doi.org/10.1016/j.mtcomm.2020.100908. URL http://www.sciencedirect.com/science/article/pii/S2352492820300143.

[52] P. Murray, G. M. Spinks, G. G. Wallace, and R. P. Burford. In-situ mechanical properties of tosylate doped (pts) polypyrrole. *Synthetic Metals*, 84(1):847–848, 1997. ISSN 0379-6779. doi: https://doi.org/10.1016/S0379-6779(96)04177-X. URL https://www.sciencedirect.com/science/article/pii/S037967799604177X.

[53] Orhan Uzun, Necati Başman, Cemil Alkan, Uğur Kölemen, and Fikret Yılmaz. Investigation of mechanical and creep properties of polypyrrole by depth-sensing indentation. *Polymer Bulletin*, 66(5):649–660, 2011. ISSN 1436-2449. doi: 10.1007/s00289-010-0361-3. URL https://doi.org/10.1007/s00289-010-0361-3.

[54] A. Kivilo, Z. Zondaka, A. Kesküla, P. Rasti, T. Tamm, and R. Kiefer. Electrochemo-mechanical deformation properties of polypyrrole/dodecylbenzenesulfate linear actuators in aqueous and organic electrolyte. *RSC Adv.*, 6:96484–96489, 2016. doi: 10.1039/C6RA20766A. URL http://dx.doi.org/10.1039/C6RA20766A.

[55] Zane Zondaka, Madis Harjo, Mahdi Safaei Khorram, Pejman Rasti, Tarmo Tamm, and Rudolf Kiefer. Polypyrrole/carbide-derived carbon composite in organic electrolyte: Characterization as a linear actuator. *Reactive and Functional Polymers*, 131:414–419, 2018. ISSN 1381-5148. doi: https://doi.org/10.1016/j.reactfunctpolym.2018.08.020. URL https://www.sciencedirect.com/science/article/pii/S1381514818307910.

[56] Jennifer L. Hicks, Thomas K. Uchida, Ajay Seth, Apoorva Rajagopal, and Scott L. Delp. Is my model good enough? best practices for verification and validation of musculoskeletal models and simulations of movement. *Journal of Biomechanical Engineering*, 137(2), 2015. ISSN 0148-0731. doi: 10.1115/1.4029304. URL https://doi.org/10.1115/1.4029304.

[57] Christelle Robinet, Robbert van den Dool, Dorian Collot, and Jacob C. Douma. Modelling for risk and biosecurity related to forest health. *Emerging Topics in Life Sciences*, 4(5):485–495, 09 2020. ISSN 2397-8554. doi: 10.1042/ETLS20200062. URL https://doi.org/10.1042/ETLS20200062.

[58] Diana C. Resasco, Fei Gao, Frank Morgan, Igor L. Novak, James C. Schaff, and Boris M. Slepchenko. Virtual cell: computational tools for modeling in cell biology. *WIREs Systems Biology and Medicine*, 4(2):129–140, 2012. doi: https://doi.org/10.1002/wsbm.165. URL https://onlinelibrary.wiley.com/doi/abs/10.1002/wsbm.165.

[59] Francisco Thiago Sacramento Aragão, Diego Arthur Hartmann, Yong-Rak Kim, Laura Maria Goretti da Motta, and Mohammad Haft-Javaherian. Numerical–experimental approach to characterize fracture properties of asphalt mixtures at low temperatures. *Transportation Research Record*, 2447(1):42–50, 2014. ISSN 0361-1981. doi: 10.3141/2447-05. URL https://doi.org/10.3141/2447-05.

[60] Becker, Joanne, Mermoz, Emmanuel, and Linares, Jean-Marc. Determination of biological joint reaction forces from in-vivo experiments using a hybrid combination of biomechanical and mechanical engineering software. *Mechanics & Industry*, 21 (6):623, 2020. doi: 10.1051/meca/2020088. URL https://doi.org/10.1051/meca/2020088.

[61] Steffen Vagts, Josef Schlattmann, Philipp Busshardt, Thomas Kleinteich, and Stanislav N. Gorb. The application of multi-body simulation approach in the kinematic analysis of beetle leg joints. *Artificial Life and Robotics*, 22(4):412–420, 2017. ISSN 1614-7456. doi: 10.1007/s10015-017-0386-x. URL https://doi.org/10.1007/s10015-017-0386-x.

[62] H. Rajabi, A. Shafiei, A. Darvizeh, S. N. Gorb, V. Dürr, and J.-H. Dirks. Both stiff and compliant: morphological and biomechanical adaptations of stick insect antennae for tactile exploration. *Journal of The Royal Society Interface*, 15(144):20180246, 2018. doi: doi:10.1098/rsif.2018.0246. URL `https://royalsocietypublishing.org/doi/abs/10.1098/rsif.2018.0246`.

[63] L. J. Jiang, J. H. Campbell, Y. F. Lu, T. Bernat, and N. Petta. Direct writing target structures by two-photon polymerization. *Fusion Science and Technology*, 70(2):295–309, 2016. ISSN 1536-1055. doi: 10.13182/FST15-222. URL `https://doi.org/10.13182/FST15-222`.

[64] Wen Zheng, Philip G Whitten, and Geoffrey M. Spinks. Polypyrrole actuators: the effects of polymer thickness and voltage scan rate on fractional charging and isotonic actuation strain. *Multifunctional Materials*, 1(1):014002, okt 2018. doi: 10.1088/2399-7532/aae3e0.

[65] Richard Guy Compton and Craig E Banks. *Understanding voltammetry*. World Scientific, 2018. ISBN 1786345285.

[66] Indrek Must, Edoardo Sinibaldi, and Barbara Mazzolai. A variable-stiffness tendril-like soft robot based on reversible osmotic actuation. *Nature Communications*, 10 (1):344, 2019. ISSN 2041-1723. doi: 10.1038/s41467-018-08173-y. URL `https://doi.org/10.1038/s41467-018-08173-y`.

Aknowledgements

The author of this work would like to thank her supervisors Indrek Must, PhD, and Tarmo Tamm, PhD, for their attentive, inspiring and supportive co-operation and supervision. Furthermore, the author would like to thank all other colleagues at IMS lab for their help and support (especially Pille Rinne, MSc, and Urmas Johanson, PhD).

This work would not have been possible without the help and support of Italian Institute of Technology Bioinpired Soft Robotics group, especially Edoardo Sinibaldi, PhD, Isabella Fiorello and Barbara Mazzolai, PhD. Thanks to other IIT colleagues is given as well.

The author would like thank her family and friends for support.

This work was financed by the Estonian Ministry of Eduaction and Research with Kristjan Jaak study period abroad scholarship and European Union European Regional Development Fund with Dora Plus program (both applied via Archimedes Foundation).

Appendix 1. *Joint Simulation Extras*

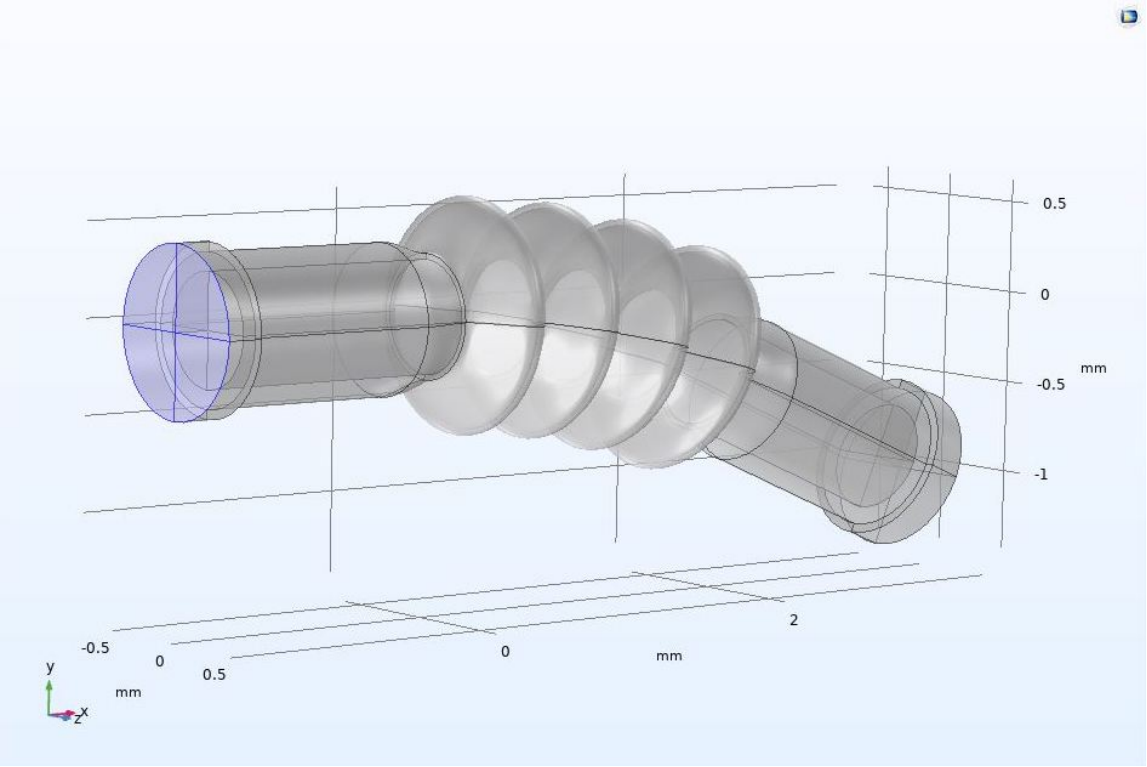

FIGURE 14: Fixed constraint area used in COMSOL simulations is showed in light blue.

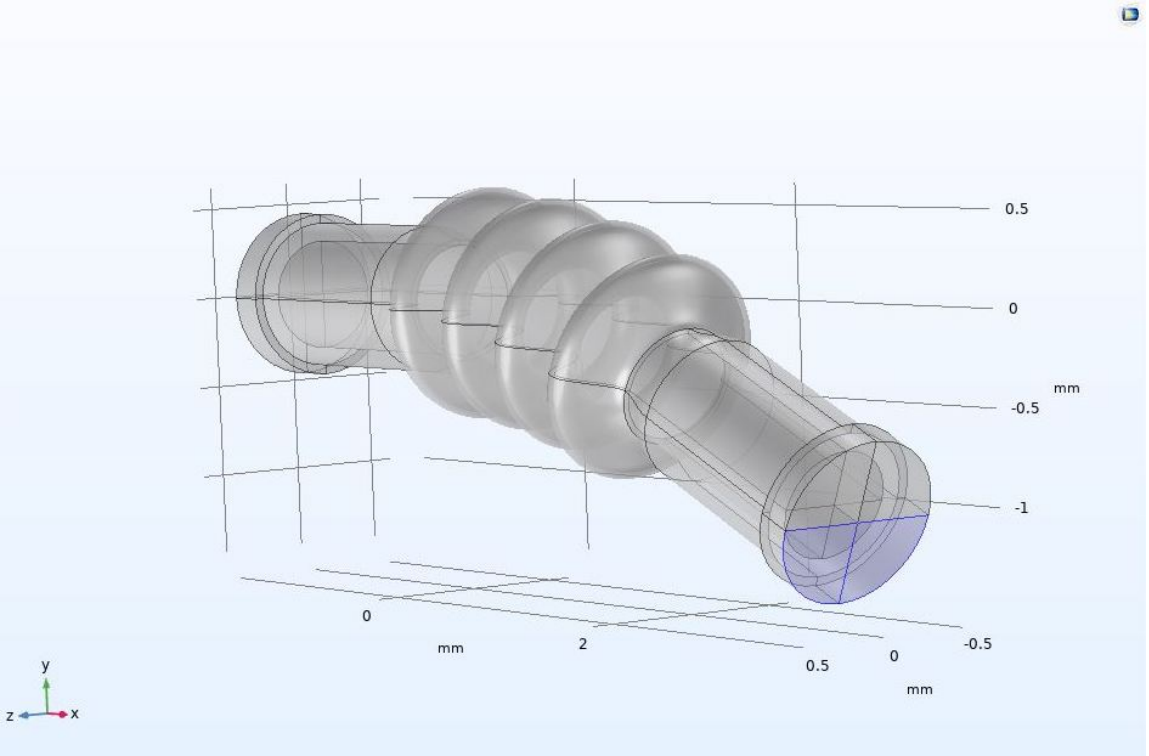

FIGURE 15: The boundary load area used in COMSOL simulations to imitate the pulling force of the PPy muscle is showed in light blue.

TABLE 1: To-bend configuration

No	Name	Expression	Description
1	len	1.5[mm]	length of links
2	lenBellows	2[mm]	length of joint
3	lenCyl	1.2[mm]	cyl length (links)
4	curv	0.2[1/mm]	curvature of mid segment
5	rIn	0.3[mm]	inner (channel) radius
6	thLarge	0.1[mm]	larger thickness
7	thSmall	0.03[mm]	smaller thickness
8	Nb	4	No of bellows
9	alpha1	0.9	sf#1 for a(s) bellows
10	alpha2	0.9	sf#2 for a(s) bellows
11	alpha3	0.9	sf for b(s) bellows
12	fTip	1.5e-3[kg]*g_const	tip force
13	lenTap	0.2[mm]	tap length (fictitious)
14	rTap	0.45[mm]	
15	rhoCurv	1/curv	curvature radius
16	thetaMid	lenBellows*curv [rad]	ang span of midsegment
17	vx	cos(thetaMid)	x, tangent versor distal link
18	vy	-sin(thetaMid)	y, tangent versor distal link
19	wx	-vy	x, normal
20	wy	vx	y, normal
21	r0	rIn+thSmall	
22	xA	-len	
23	xB	-len+lenCyl	
24	xP	rhoCurv*sin(thetaMid)	
25	yP	rhoCurv*(cos(thetaMid)-1)	
26	xC	xP+vx*(len-lenCyl)	
27	yC	yP+vy*(len-lenCyl)	
28	xD	xP+vx*len	
29	yD	yP+vy*len	
30	areaLoad	0.5*pi*(rTap^2)	tap area (fictitious)
31	pTap	fTip/areaLoad	tap pressure (fictitious)
32	deltaTh	thLarge-thSmall	

TABLE 2: To-straighten configuration

No	Name	Expression	Description
1	len	1.5[mm]	length of links
2	lenBellows	2[mm]	length of joint
3	lenCyl	1.2[mm]	cyl length (links)
4	curv	0.6[1/mm]	curvature of mid segment
5	rIn	0.3[mm]	inner (channel) radius
6	thLarge	0.1[mm]	larger thickness
7	thSmall	0.03[mm]	smaller thickness
8	Nb	4	No of bellows
9	alpha1	1.25	sf#1 for a(s) bellows
10	alpha2	1.25	sf#2 for a(s) bellows
11	alpha3	0	sf for b(s) bellows
12	fTip	1.5e-3[kg]*g_const	tip force
13	lenTap	0.2[mm]	tap length (fictitious)
14	rTap	0.45[mm]	
15	rhoCurv	1/curv	curvature radius
16	thetaMid	lenBellows*curv [rad]	ang span of midsegment
17	vx	cos(thetaMid)	x, tangent versor distal link
18	vy	-sin(thetaMid)	y, tangent versor distal link
19	wx	-vy	x, normal
20	wy	vx	y, normal
21	r0	rIn+thSmall	
22	xA	-len	
23	xB	-len+lenCyl	
24	xP	rhoCurv*sin(thetaMid)	
25	yP	rhoCurv*(cos(thetaMid)-1)	
26	xC	xP+vx*(len-lenCyl)	
27	yC	yP+vy*(len-lenCyl)	
28	xD	xP+vx*len	
29	yD	yP+vy*len	
30	areaLoad	0.5*pi*(rTap^2)	tap area (fictitious)
31	pTap	fTip/areaLoad	tap pressure (fictitious)
32	deltaTh	thLarge-thSmall	

Non-exclusive licence to reproduce thesis and make thesis public

I, Kadri-Ann Valdur,

1. herewith grant the University of Tartu a free permit (non-exclusive licence) to:
   (a) reproduce, for the purpose of preservation, including for adding to the DSpace digital archives until the expiry of the term of copyright, and
   (b) make available to the public via the web environment of the University of Tartu, including via the DSpace digital archives, under the Creative Commons licence CC BY NC ND 3.0, which allows, by giving appropriate credit to the author, to reproduce, distribute the work and communicate it to the public, and prohibits the creation of derivative works and any commercial use of the work from **04.06.2024** until the expiry of the term of copyright,

   A mm-scale liquid-enabled robotic exoskeleton,

   Supervised by Indrek Must and Tarmo Tamm,
2. I am aware of the fact that the author retains the rights specified in p. 1
3. I certify that granting the non-exclusive licence does not infringe other persons' intellectual property rights or rights arising from the personal data protection legislation.

Kadri-Ann Valdur

Tartu, June 4, 2021